

ViEEG: Hierarchical Visual Neural Representation for EEG Brain Decoding

Minxu Liu¹, Donghai Guan^{1,*}, Chuhang Zheng², Chunwei Tian³, Jie Wen⁴, Qi Zhu²,

¹College of Computer Science and Technology, Nanjing University of Aeronautics and Astronautics,

²College of Artificial Intelligence, Nanjing University of Aeronautics and Astronautics,

³Harbin Institute of Technology, ⁴Harbin Institute of Technology, Shenzhen

liuminxu@nuaa.edu.cn, dhguan@nuaa.edu.cn, h.zheng@nuaa.edu.cn, chunweitian@163.com, jiewen_pr@126.com, zhuqinuaa@163.com

Abstract

Understanding and decoding brain activity into visual representations is a fundamental challenge at the intersection of neuroscience and artificial intelligence. While EEG visual decoding has shown promise due to its non-invasive, and low-cost nature, existing methods suffer from **Hierarchical Neural Encoding Neglect (HNEN)**—a critical limitation where flat neural representations fail to model the brain’s hierarchical visual processing hierarchy. Inspired by the hierarchical organization of visual cortex, we propose **ViEEG**, a neuro-inspired framework that addresses HNEN. ViEEG decomposes each visual stimulus into three biologically aligned components—contour, foreground object, and contextual scene—serving as anchors for a three-stream EEG encoder. These EEG features are progressively integrated via cross-attention routing, simulating cortical information flow from low-level to high-level vision. We further adopt hierarchical contrastive learning for EEG-CLIP representation alignment, enabling zero-shot object recognition. Extensive experiments on the THINGS-EEG dataset demonstrate that ViEEG significantly outperforms previous methods by a large margin in both subject-dependent and subject-independent settings. Results on the THINGS-MEG dataset further confirm ViEEG’s generalization to different neural modalities. Our framework not only advances the performance frontier but also sets a new paradigm for EEG brain decoding.

1 Introduction

Electroencephalogram (EEG) visual decoding aims to bridge the gap between cortical dynamics and machine perception by reconstructing visual experiences from brain activity (Du et al. 2023). As a pivotal modality in brain-computer interfaces, EEG (Craik, He, and Contreras-Vidal 2019) has gained prominence due to its cost-effectiveness, portability, and millisecond-level temporal resolution. Recent years have witnessed substantial progress in EEG visual decoding methodologies (Liu et al. 2024; Bai et al. 2023; Fu et al. 2025). However, unlike functional magnetic resonance imaging (fMRI) signals (Worsley et al. 2002) that have established sophisticated decoding frameworks (Zafar et al. 2015; Sun et al. 2023; Horikawa and Kamitani 2017; Zhou et al. 2024), EEG visual decoding remains in infancy, with significant challenges unaddressed, particularly in modeling the brain hierarchical visual processing mechanisms.

* Corresponding author

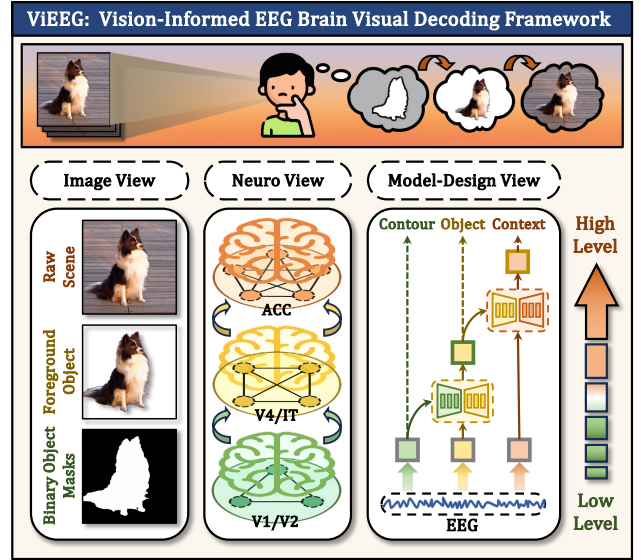


Figure 1: Triple-view hierarchical visual decoding.

Contemporary EEG decoding approaches predominantly establish direct visual-semantic mappings between EEG and stimulus images. For instance, Mb2C (Wei et al. 2024) employed contrastive learning for direct EEG-image embedding alignment with contrastive language-image pretraining (CLIP) (Radford et al. 2021; Ramesh et al. 2022), while NICE (Song et al. 2024) developed spatiotemporal neural architectures tailored for EEG visual decoding. Recent innovations include incorporating brain topological connectivity (Li et al. 2024) and integrating multimodal semantic cues (Zhang et al. 2024). Despite these advancements, most existing methods overlook a fundamental property of the human visual system: its hierarchical nature. We term this issue as Hierarchical Neural Encoding Neglect (HNEN). Rooted in the canonical hierarchical cortical processing pathway, the human visual system processes stimuli through dissociable stages: from low-level edge detection to high-level semantic integration (Felleman and Van Essen 1991; Riesenhuber and Poggio 1999). In contrast, existing methods collapse biological hierarchy into flat representation learning, resulting in incomplete visual information capturing.

Substantial neuroscientific evidence (Ben-Yishai, Bar-

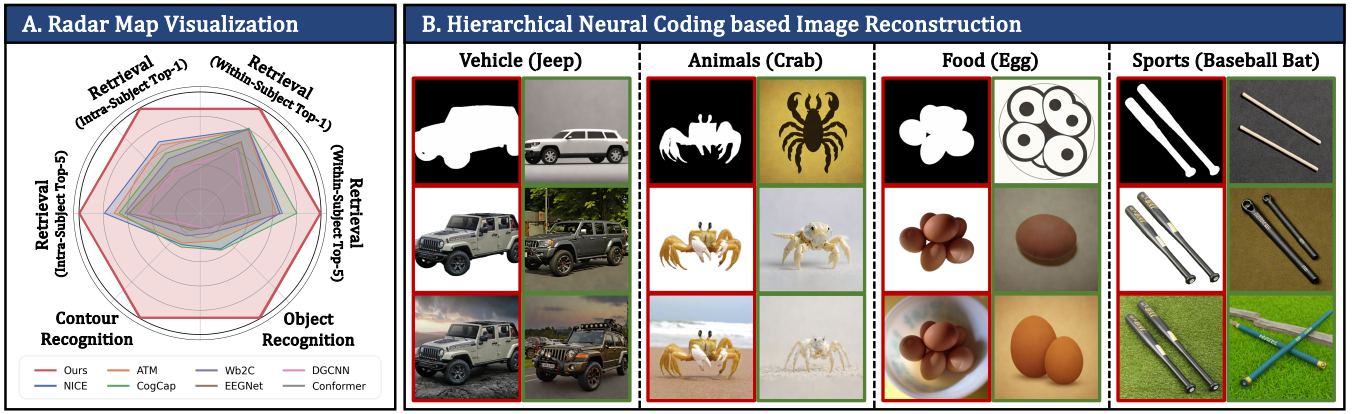


Figure 2: EEG brain visual decoding of ViEEG. In subgraph. B, red: ground-trues images; green: EEG reconstructed images..

Or, and Sompolinsky 1995; Li, Todo, and Tang 2022) supports a hierarchically organized cortical visual pathway for visual perception: The early visual cortex ($V1^1/V2^2$ (Bridge et al. 2005)) specializes in elementary low-level feature extraction (e.g., edge contours), the intermediate ventral stream ($V4^3/IT^4$ (Hansen, Kay, and Gallant 2007; Arcaro and Livingstone 2021)) processes object-level semantics, while higher-order association cortex correlates⁵ (Grill-Spector and Malach 2004) integrate high-level contextual scene understanding. This hierarchical visual decoding enables humans to progressively distill visual information—from coarse contours to fine-grained semantics—through layered cortical interactions. However, existing EEG brain decoding methods adopt a monolithic processing paradigm that adopts a flat representation paradigm that collapses biological hierarchy. By attempting direct mappings between EEG and holistic image embeddings, these approaches suffer from HNEN, failing to distinguish:

- Contour edge saliency ($V1/V2$ correlates)
- Foreground-object-centric semantics ($V4/IT$ correlates)
- Contextual scene attributes (AC correlates)

The absence of cortically-aligned feature disentanglement fundamentally limits the capacity to localize visual saliency, particularly in preserving contour fidelity.

Our proposed **vision-informed EEG (ViEEG)** brain decoding framework addresses HNEN through hierarchical visual decoding, as can be seen in Figure 1. We architect three complementary processing layers: (1) **Contour Priming Layer** where binary object masks guide EEG feature extraction for edge saliency, (2) **Object Purification Layer** that isolates foreground object semantics and purges background, and (3) **Contextual Integration Layer** capturing association cortex-level scene understanding from raw image. Three parallel spatiotemporal encoders decode EEG signals following the **hierarchical visual comprehension**

(Contour \rightarrow Object \rightarrow Context), progressively integrating features through cross-attention mechanisms. The mask-constrained modules extract edge gradients, the object-centric attention refines core semantics, and the cross-stream fusion gates integrate contextual cues. Hierarchical CLIP anchoring reinforces biological plausibility: mask embeddings align with contour EEG patterns to preserve shape fidelity, object embeddings couple with foreground semantic features to suppress background interference, and raw image embeddings bind with contextual dynamics to maintain scene coherence. This structured mimicry of visual processing stages—from low-level edge detection to high-level semantic comprehension—directly resolves the HNEN and flat representation bottleneck in conventional approaches through biologically-grounded feature disentanglement.

Our main contributions can be summarized as follows:

- **A biologically-inspired hierarchical framework** for EEG visual decoding, pioneering tri-stream modeling (Contour \rightarrow Object \rightarrow Context). To our knowledge, this is the first work to explicitly enforce feature disentanglement along the visual cortical hierarchy.
- **A novel cross-attention routing mechanism** that integrates multilevel EEG features via bottom-up hierarchical attention, enabling effective contour-object-contextual information fusion.
- **Bidirectional neuro-AI validation**, showing how neuroscientific theory can guide model design, while our decoding results, in turn, support biologically plausible brain representations.
- **New state-of-the-art performance** on THINGS-EEG: achieving 40.9% Top-1 ($\uparrow 49.82\%$) in subject-dependent and 22.9% Top-1 ($\uparrow 45.86\%$) in cross-subject settings, substantially outperforming previous benchmarks.

2 Related Works

Decoding the brain’s response to visual stimuli has been a central pursuit in neuroscience and brain-computer interface (BCI) research (Lee, Lee, and Lee 2020; Shi et al. 2024; Liu et al. 2025). Early efforts predominantly focused on fMRI visual decoding (Allen et al. 2022; Huo et al. 2024),

¹Primary visual cortex ($V1$): basic edge detection and orientation processing

²Secondary visual cortex ($V2$): local contours and complex shapes integration

³Visual Area 4 ($V4$): shape/color information processing

⁴Inferotemporal Cortex (IT): object recognition and semantic categorization

⁵Association Cortex Correlates (AC): Contextual scene understanding integration

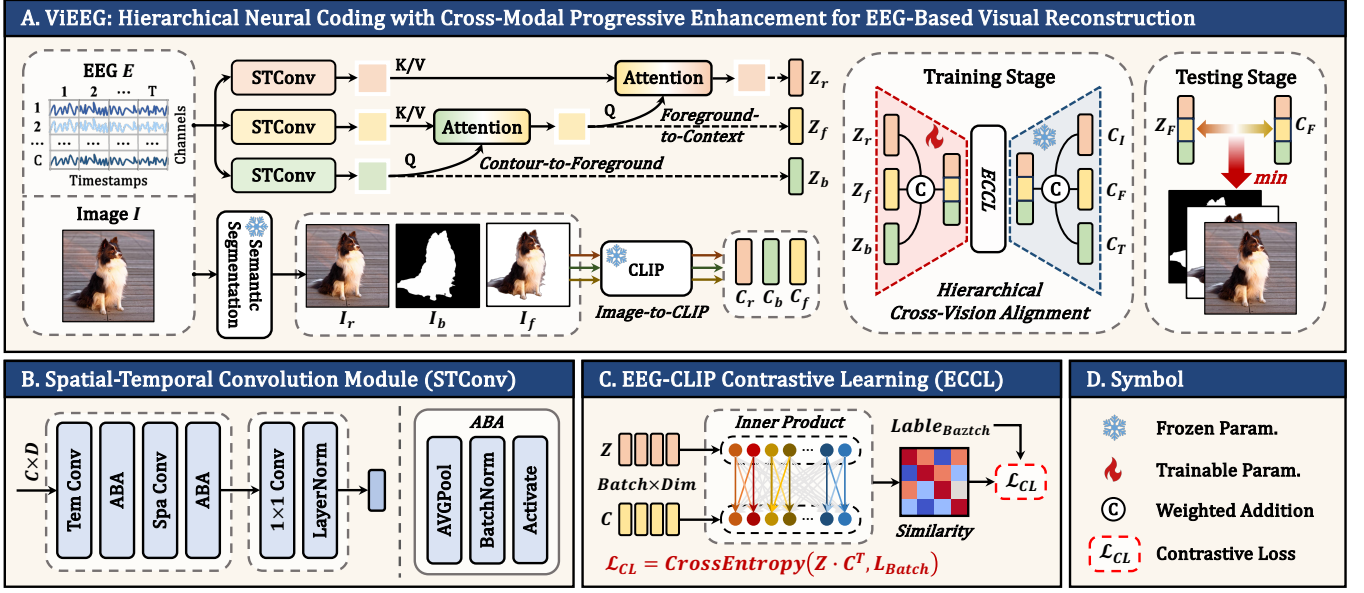


Figure 3: Overview of the ViEEG framework. The input image is decomposed into three biologically inspired views: binary mask, foreground object, and raw scene. Corresponding EEG responses are encoded by parallel spatiotemporal encoders, integrated via hierarchical cross-attention, and aligned with CLIP embeddings through hierarchical contrastive learning.

where high spatial resolution inherently captures hierarchical visual processing. For instance, MindEye (Scotti et al. 2023), proposed to map fMRI to CLIP features via diffusion models, while MindBridge (Wang et al. 2024) developed to align fMRI with images and textual captions. These methods leverage fMRI’s spatial precision to distinguish low-level (e.g., edges) and high-level (e.g., semantics) visual features implicitly, even when relying on simplistic alignment.

In contrast, the spatial ambiguity of the EEG centimeter scale forces existing methods (Rakhimberdina et al. 2021; Song et al. 2024) into flat representation paradigms that confuse hierarchical visual processing. As the dominant brain decoding approach of fMRI and EEG, direct EEG-image alignment fails to model the brain’s progressive refinement from edges to semantics, a limitation we term HNEN. While some attempts incorporate electrode topology (Li et al. 2024) or depth cues (Zhang et al. 2024), these merely address symptoms (e.g., spatial noise) rather than HNEN’s root cause: EEG’s inability to functionally isolate cortical processing stages. This divergence highlights a critical gap: fMRI passively inherits hierarchical decoding through anatomy, whereas EEG demands active hierarchy simulation. Our proposed ViEEG bridges the gap via artificial cortical anchors—decomposing images into low-level edge masks, foreground entities, and high-level contextual scenes. By enforcing hierarchical EEG embedding disentanglement, we circumvent EEG’s spatial limitations while aligning with biological visual processing—a novel paradigm transcending both fMRI’s anatomy-dependence and EEG’s flat representations.

3 Method

3.1 Preliminaries

The core components of the proposed ViEEG framework are summarized in Table 1, where each symbol is defined based on both computational roles and neuroscientific alignment.

Symbol	Dim.	Definition
E	$R^{C \times T}$	Raw EEG signals
I	$R^{H \times W}$	Raw image
I_b	$R^{D \times D}$	Binary object mask image
I_f	$R^{D \times D}$	Foreground object image
I_r	$R^{D \times D}$	Raw scene image
F_b, F_f, F_r	R^d	Contour/object/context EEG embedding
C_b, C_f, C_r	R^d	Contour/object/context CLIP embedding

Table 1: Key symbol definitions. C : EEG channels, T : time-points, $H \times W$: image resolution, $D \times D$: reshaped image resolution (512), d : embedding dimension (1024).

We formulate EEG visual decoding as a hierarchical zero-shot object recognition, where test categories are disjoint from the training set. Given EEG recordings E with N samples elicited by visual stimuli $\{I_b, I_f, I_r\}$, our objective is to learn hierarchical EEG embeddings $\{F_b, F_f, F_r\}$ that align with the corresponding CLIP embeddings $\{C_b, C_f, C_r\}$ through hierarchical visual decoding. The learning objective for zero-shot object recognition is formulated as:

$$\min_{\theta} \frac{1}{N} \sum_{i=1}^N D(F^i, C^i), \quad (1)$$

where $D(\cdot, \cdot)$ measures feature similarity. On the THINGS-EEG dataset, we train with class-disjoint stimuli and test on unseen categories. At inference time, the concatenated EEG

embeddings F_b, F_f, F_r are compared to CLIP embeddings using cosine similarity within an InfoNCE-style contrastive learning framework (Radford et al. 2021).

3.2 Overall Architecture

ViEEG introduces a biologically inspired hierarchical architecture for EEG visual decoding, simulating layered cortical processing. As illustrated in Figure 2, ViEEG comprises three synergistic components: (1) Hierarchical image decomposition, (2) Hierarchical EEG encoding, and (3) Hierarchical Contrastive Learning. During initialization, we extract CLIP embeddings from the three decomposed visual representations. In the training phase, EEG features extracted from EEG encoder are aligned with the image CLIP embeddings using contrastive learning. During testing, EEG embeddings extracted from the test set are matched to target samples based on similarity measurements for evaluation.

3.3 Hierarchical Image Decomposition

Inspired by the hierarchical structure of the human visual system, we decompose each stimulus image I into three biologically aligned representations via semantic segmentation.

Step 1: Image Processing. We employ the pre-trained BiRefNet⁶ (Zheng et al. 2024), a state-of-the-art high-resolution segmentation model, to generate hierarchical visual representations. The raw image I is first normalized to yield I_r , ensuring consistent dimensions and intensity scaling. Saliency detection is then applied, and a binary contour representation is obtained via thresholding:

$$I_b = I(\mathcal{F}_{\text{BiRefNet}}(I_r) > \tau) \quad (2)$$

where $\mathcal{F}_{\text{BiRefNet}}$ denotes the pre-trained BiRefNet model, $I(\cdot)$ is the indicator function, and τ is threshold value. The resulting I_b serves as a binary object mask that highlights salient contours. Next, to extract the foreground object, we perform element-wise multiplication:

$$I_f = I_r \odot I_b \quad (3)$$

where \odot is element-wise multiplication, and yielding I_f , the foreground object image with the background suppressed.

Step 2: Image CLIP Embedding Processing. To capture semantic information from each image representation, we utilize a frozen CLIP-ViT-H/14 to extract embeddings as:

$$C_b = \text{CLIP}(I_b), \quad C_f = \text{CLIP}(I_f), \quad C_r = \text{CLIP}(I_r) \quad (4)$$

where C_b, C_f , and C_r represent the embeddings corresponding to the binary mask, foreground object, and raw scene image, respectively. These embeddings serve as the foundation for subsequent hierarchical contrastive learning with EEG.

3.4 Hierarchical EEG Encoding

Our neuro-inspired encoding architecture extracts hierarchical (contour/object/context) EEG features. Given raw EEG E , three parallel streams extract cortical hierarchy-aligned EEG features through spatiotemporal convolution (STConv) and cross-attention hierarchical integration (CAHI).

3.5 Spatiotemporal Convolution

To extract meaningful spatiotemporal representations from EEG signals, we employ a multi-stage convolutional processing pipeline. The first stage applies temporal convolution using a kernel of size $(1, K_t)$ and a stride of S_t , capturing temporal dependencies across EEG signals. This is followed by an average pooling operation with a kernel size of $(1, K_p)$ and a stride of S_p , which reduces temporal resolution while preserving crucial information. The second stage applies spatial convolution across electrodes using a kernel size of $(C, 1)$, performing spatial filtering. The processed features are then normalized and activated through an ELU function before being projected into the final hierarchical feature representation:

$$\begin{aligned} F^{(1)} &= \text{ELU}(\text{BatchNorm}(\text{AvgPool}(\text{Conv2D}_t(E)))) \\ F^{(2)} &= \text{ELU}(\text{BatchNorm}(\text{Conv2D}_s(F^{(1)}))) \\ F^0 &= \text{Conv2D}_{proj}(F^{(2)}) \end{aligned} \quad (5)$$

where $\text{Conv2D}_t(\cdot)$ is temporal convolution, $\text{Conv2D}_s(\cdot)$ represents spatial convolution, and $\text{Conv2D}_{proj}(\cdot)$ is a 1×1 convolution. These hierarchical spatiotemporal features facilitate robust representation learning, which is further refined through the cross-attention mechanism. After three parallel STConv operations, EEG signals are decoupled into three features: F_b^0, F_f^0 , and F_r^0 .

3.6 Cross-Attention Hierarchical Integration (CAHI)

The CAHI integrates biologically inspired features through contour-to-object and object-to-context integration. Since contour features can enhance object features, and object features provide additional context information, we integrate these two integration processes accordingly. Assuming that low-level representation is denoted by a and higher-level representation by b , we perform bottom-up integration, and transfer information from a to b . We use a and apply several linear transformations to generate key embeddings in attention, while generate query and value embeddings from b as:

$$K^i = a^i W^K, \quad Q^i = b^i W^Q, \quad V^i = a^i W^V \quad (6)$$

where a^i represents the i -th attention head, and W^Q, W^K , and W^V are the parameter matrices for Q^i, K^i , and V^i , respectively. We determine the attention coefficients by computing the scaled dot-product between Q and K , followed by a softmax to obtain the attention weights. The final feature for each head is computed as:

$$F^i = \text{Attention}(Q^i, K^i, V^i) = \text{softmax}\left(\frac{Q^i K^{iT}}{\sqrt{d}}\right) V^i \quad (7)$$

where d is the normalization hyperparameter. The output of the multi-head self-attention is then given by:

$$F = \text{MHA}(K = a, Q = V = b) = (F^1 \| F^2 \| \dots \| F^h) W^O + b \quad (8)$$

where $\text{MHA}(\cdot)$ denote multi-head attention function, h is the number of attention heads, W^O is a linear transformation, and $\|$ denotes concatenation.

⁶<https://huggingface.co/ZhengPeng7/BiRefNet>

Contour-to-Object Integration: The low-level and high-level representation is contour feature F_b^0 and object feature F_f^0 , respectively, and refined object feature is computed as:

$$F_f = \text{LN}\left(F_f^0 + \text{Dropout}\left(\text{MHA}(K = F_b^0, Q = V = F_f^0)\right)\right) \quad (9)$$

where $\text{LN}(\cdot)$ is the LayerNorm function.

Object-to-Context Integration: The low-level and high-level representation is object feature F_f^0 and context feature F_r^0 , respectively, and refined context feature is computed as:

$$F_r = \text{LN}\left(F_r^0 + \text{Dropout}\left(\text{MHA}(K = F_f^0, Q = V = F_r^0)\right)\right) \quad (10)$$

3.7 Hierarchical Contrastive Learning

To further enhance representation learning, we adopt a contrastive learning framework that aligns the concatenated EEG features with their corresponding image embeddings. Specifically, we first concatenate the hierarchical EEG features, i.e., $F_{\text{eeg}} = (F_b \| F_f \| F_r)$, and similarly, the image features are concatenated as $C_{\text{img}} = (C_b \| C_f \| C_r)$. We then compute the cosine similarity between these concatenated features, scaled by a learnable temperature parameter α (with $\alpha = \exp(\text{logit_scale})$). The final loss is computed as the cross-entropy loss on the resulting similarity logits:

$$\mathcal{L} = \text{CrossEntropy}(\alpha \cdot \cos(F_{\text{eeg}}, C_{\text{img}}), Y) \quad (11)$$

where $\cos(\cdot, \cdot)$ is cosine similarity function, and Y denotes the ground-truth labels. This formulation encourages the EEG features to closely align with the corresponding image features in the shared embedding space.

4 Experiment

4.1 Dataset

The **THINGS-EEG** dataset (Gifford et al. 2022) is the large-scale benchmark and the most widely used in zero-shot EEG object recognition, comprising brain responses from ten participants exposed to images from the THINGS database under a RSVP paradigm. The dataset comprises 1654 training concepts and 200 zero-shot test concepts, yielding a total of 82,160 trials per subject. EEG signals were acquired using a 64-channel cap, band-pass filtered between 0.1–100 Hz, and subsequently downsampled to 100 Hz. Preprocessing involved segmenting epochs from 200 ms before to 800 ms after stimulus onset, followed by baseline correction using the pre-stimulus interval. Additionally, we evaluate ViEEG on **THINGS-MEG** dataset (Hebart et al. 2023) in Appendix, to validate the universality across various neural signals.

4.2 Experimental Details

All experiments were implemented in PyTorch and conducted on an NVIDIA RTX 3090 (4-GPU) environment. The key hyperparameters include a mask threshold $\tau = 0.5$, temporal convolution kernel size 1×25 , spatial convolution kernel 63×1 , average pooling kernels 1×51 and 1×5 , a dropout rate of 0.5, attention layer depth of 1, and 3 attention heads. The model is optimized using Adam with a batch size of 1000 and a learning rate of 2×10^{-3} .

For fair comparison, experiments were conducted follow the protocol of NICE/ATM. All methods used the same CLIP backbone (CLIP-ViT-H/14) to ensure alignment consistency. For subject-dependent training, 740 trials were randomly selected as the validation set, and the model with the lowest validation loss was retained. For subject-independent training, we employed a leave-one-subject-out (LOSO) protocol, using 6660 trials for validation in each fold. All experiments were repeated five times, and the average test accuracy was reported to mitigate variance and ensure result robustness. **Importantly, additional experimental details, including THINGS-MEG results, extensive ablation and parameter studies, computational resource analysis, visualizations, and more image retrieval and reconstruction examples, are provided in supplementary Appendix.**

4.3 Overall Performance

The experimental comparison against state-of-the-art methods demonstrates ViEEG’s superior decoding capability across both evaluation paradigms. We conduct comprehensive comparisons against 10 EEG decoding methods, including BraVL (Du et al. 2023), LSTM (Hochreiter 1997), ConvNet (Schirrmester et al. 2017), Conformer (Song et al. 2022), DGCNN (Song et al. 2018), EEGNet (Lawhern et al. 2018), MB2C (Wei et al. 2024), NICE (Song et al. 2024), ATM (Li et al. 2024), and CognitionCapturer (Cog-Cap) (Zhang et al. 2024). Table 2 summarizes the 200-way zero-shot recognition performance across both experimental paradigms, and our method ViEEG achieves consistent improvements over existing approaches through biologically grounded hierarchical modeling.

Subject-Dependent Experiment. ViEEG achieves new performance benchmarks, reaching **40.9%** Top-1 and **74.5%** Top-5 average accuracy across 10 subjects, outperforming the previous SOTA method by substantial margins. Specifically, compared to the baseline NICE, ViEEG demonstrates an average improvement of **49.82%** in Top-1 accuracy and **24.79%** in Top-5 accuracy, reflecting its capacity to effectively exploit subject-specific neural patterns. This performance highlights ViEEG’s capacity to handle visual scenes through hierarchical feature disentanglement.

Subject-Independent Experiment. When tested on unseen subjects under LOSO protocol, ViEEG maintains robust performance with **22.9%** Top-1 and **51.4%** Top-5 accuracy. The biological plausibility of hierarchical design enables better generalization compared to flat representation. For average object recognition accuracy, ViEEG demonstrates relative improvement of **45.86%** in Top-1 accuracy and **25.06%** in Top-5 accuracy. This performance gap stems from ViEEG’s hierarchical feature disentanglement that captures invariant neural patterns across individuals.

4.4 Ablation Study

We conducted ablation study to assess the contributions of each core module in ViEEG, as summarized in Table 3.

Ablation on Hierarchical Embedding. This experiment analyzes the effectiveness of different levels of hierarchical EEG embeddings. Specifically, we evaluated configu-

Method	Subject 1		Subject 2		Subject 3		Subject 4		Subject 5		Subject 6		Subject 7		Subject 8		Subject 9		Subject 10		Ave	
	top-1	top-5	top-1	top-5	top-1	top-5	top-1	top-5	top-1	top-5	top-1	top-5	top-1	top-5	top-1	top-5	top-1	top-5	top-1	top-5	top-1	top-5
Subject dependent - train and test on one subject																						
BraVL (Du et al. 2023)	6.1	17.9	4.9	14.9	5.6	17.4	5.0	15.1	4.0	13.4	6.0	18.2	6.5	20.4	8.8	23.7	4.3	14.0	7.0	19.7	5.8	17.5
LSTM (Hochreiter 1997)	16.4	43.5	16.1	40.2	20.7	49.4	18.6	42.3	14.2	35.2	18.2	43.1	18.7	47.2	22.0	47.9	16.8	43.8	21.7	52.2	18.3	44.5
ConvNet (Schirmeister et al. 2017)	14.9	39.3	18.9	42.1	17.8	49.0	23.9	55.8	12.2	32.9	20.1	46.5	15.5	42.6	20.7	48.9	20.7	49.8	19.3	47.5	18.4	45.5
Conformer (Song et al. 2022)	11.4	32.4	15.2	41.9	19.8	50.9	23.0	56.6	13.6	33.4	18.1	49.0	18.5	48.2	27.1	56.9	15.2	40.0	22.6	57.8	18.5	46.7
DGCNN (Song et al. 2018)	12.3	36.6	11.5	39.5	15.7	43.8	19.7	50.6	10.6	32.6	15.4	46.6	14.0	43.2	25.1	54.5	16.0	43.7	17.9	53.0	15.8	44.4
EEGNet (Lawhern et al. 2018)	16.0	42.9	17.9	48.6	18.2	51.5	23.9	59.0	14.4	37.7	19.5	52.0	18.5	50.2	30.2	61.2	23.3	51.2	22.5	58.3	20.4	51.2
Mb2C (Wei et al. 2024)	23.6	56.3	22.6	50.5	26.3	60.1	34.8	67.0	21.3	53.0	31.0	62.3	25.0	54.8	39.0	69.3	27.5	59.3	33.1	70.8	28.4	60.3
NICE (Song et al. 2024)	21.7	51.2	23.3	55.0	29.1	60.5	32.3	69.6	18.2	45.6	29.3	62.1	24.3	59.2	41.3	72.4	24.3	59.0	28.9	62.6	27.3	59.7
ATM (Li et al. 2024)	25.6	60.5	22.0	54.5	25.0	62.4	31.4	60.9	12.9	43.0	21.3	51.1	30.5	61.5	38.8	72.0	24.4	51.5	29.1	63.5	26.1	58.1
CogCap (Zhang et al. 2024)	27.2	59.5	28.7	56.9	37.1	66.1	37.6	63.2	21.8	47.7	31.5	58.0	32.8	59.5	47.6	73.5	33.3	57.6	35.0	63.5	33.3	60.5
ViEEG	34.1	71.3	38.4	67.9	40.6	74.7	50.1	80.8	28.9	61.5	44.3	76.5	38.6	75.2	54.0	82.5	37.3	74.9	42.8	79.8	40.9	74.5
Subject independent - leave one subject out for test																						
BraVL (Du et al. 2023)	2.3	8.0	1.5	6.3	1.4	5.9	1.7	6.7	1.5	5.6	1.8	7.2	2.1	8.1	2.2	7.6	1.6	6.4	2.3	8.5	1.8	7.0
LSTM (Hochreiter 1997)	9.2	30.3	10.3	26.4	6.4	19.3	9.1	25.2	7.8	22.2	8.4	27.6	7.5	22.0	10.6	26.9	5.3	22.6	9.3	26.1	8.4	24.8
ConvNet (Schirmeister et al. 2017)	10.4	31.5	14.2	35.0	8.7	26.9	12.1	31.4	5.7	22.5	10.2	28.0	8.3	22.5	10.0	29.9	6.6	19.8	12.2	34.0	9.8	28.2
Conformer (Song et al. 2022)	6.3	22.3	5.7	20.4	5.8	15.7	7.8	21.8	6.7	18.4	10.4	32.9	7.0	24.1	9.1	25.2	5.0	17.2	11.7	33.2	7.5	23.1
DGCNN (Song et al. 2018)	10.8	30.6	11.9	31.3	6.3	21.3	8.2	24.6	6.1	18.5	11.2	30.4	6.8	20.5	11.0	28.6	9.4	25.4	12.2	30.6	9.4	26.2
EEGNet (Lawhern et al. 2018)	11.0	31.1	11.4	34.0	6.5	24.7	13.4	34.4	6.7	26.7	8.5	29.4	7.9	22.0	10.7	32.9	8.9	27.7	15.1	41.6	10.0	30.4
Mb2C (Wei et al. 2024)	10.5	28.1	11.3	32.8	8.8	27.6	13.6	33.5	10.6	27.5	12.1	33.1	11.5	31.8	12.0	32.1	12.1	31.3	16.1	42.1	11.9	32.0
NICE (Song et al. 2024)	13.5	39.3	16.7	42.7	12.4	35.5	17.9	41.9	14.7	38.1	15.6	44.6	13.6	39.0	13.5	37.2	17.0	42.0	22.8	50.7	15.7	41.1
ATM (Li et al. 2024)	17.1	41.8	20.2	44.2	13.2	36.7	17.0	40.7	15.1	41.0	13.5	38.3	10.1	29.0	15.2	41.9	13.5	38.4	20.0	45.4	15.5	39.6
CogCap (Zhang et al. 2024)	16.3	42.3	16.2	37.9	8.8	26.8	15.4	37.6	10.1	31.7	14.0	35.4	10.7	26.9	13.9	34.2	9.0	32.4	15.3	38.6	13.0	34.4
ViEEG	22.7	53.5	24.7	52.5	19.0	48.4	25.5	54.1	19.8	47.3	20.7	49.3	20.9	49.4	20.8	46.8	23.8	52.7	31.2	60.3	22.9	51.4

Table 2: Overall accuracy (%) comparison: Top-1 and Top-5 in 200-way zero-shot object recognition.

Method	Subject 1		Subject 2		Subject 3		Subject 4		Subject 5		Subject 6		Subject 7		Subject 8		Subject 9		Subject 10		Ave	
	top-1	top-5	top-1	top-5	top-1	top-5	top-1	top-5	top-1	top-5	top-1	top-5	top-1	top-5	top-1	top-5	top-1	top-5	top-1	top-5	top-1	top-5
Subject dependent - train and test on one subject																						
F_b Feature Only	14.2	41.8	14.0	39.8	17.0	39.1	20.9	53.2	8.6	30.3	13.6	40.9	14.7	40.7	17.6	46.4	12.8	37.6	14.8	44.0	14.8	41.4
F_f Feature Only	22.2	52.1	24.5	56.1	29.9	66.0	34.0	67.1	19.2	50.0	32.5	63.5	26.5	58.7	38.7	73.9	29.3	61.8	31.8	68.5	28.9	61.8
F_r Feature Only	22.1	52.6	24.8	58.0	32.4	62.7	33.1	67.4	18.5	49.1	29.7	66.2	26.8	60.1	40.6	74.1	27.4	62.5	31.8	68.6	28.6	62.1
w/o Cross-Attention	32.4	66.8	34.6	65.9	39.1	71.3	46.5	80.2	27.2	59.8	40.5	74.3	35.3	71.3	52.2	80.8	34.6	71.9	43.9	75.5	38.6	71.8
ViEEG	34.1	71.3	38.4	67.9	40.6	74.7	50.1	80.8	28.9	61.5	44.3	76.5	38.6	75.2	54.0	82.5	37.3	74.9	42.8	79.8	40.9	74.5
Subject independent - leave one subject out for test																						
F_b Feature Only	5.9	18.6	7.9	22.7	5.7	19.1	7.4	26.3	7.6	20.5	4.2	18.6	9.0	23.1	7.9	21.8	7.0	20.8	10.2	30.9	7.3	22.3
F_f Feature Only	15.8	43.0	19.8	42.5	13.3	40.3	20.5	45.1	13.7	37.1	17.1	41.7	13.2	39.7	15.5	41.9	15.3	42.9	23.4	51.4	16.8	42.6
F_r Feature Only	14.9	41.5	18.4	45.9	14.1	41.3	18.1	42.2	15.9	38.3	18.5	42.8	15.4	41.5	16.0	41.6	18.3	45.3	20.5	50.2	17.0	43.1
w/o Cross-Attention	19.1	52.1	22.0	48.9	15.1	45.1	24.2	55.2	16.7	41.6	21.0	50.4	17.2	44.7	19.5	45.6	20.9	48.8	31.1	59.8	20.7	49.2
ViEEG	22.7	53.5	24.7	52.5	19.0	48.4	25.5	54.1	19.8	47.3	20.7	49.3	20.9	49.4	20.8	46.8	23.8	52.7	31.2	60.3	22.9	51.4

Table 3: Ablation study: Top-1 and Top-5 accuracy (%) in 200-way zero-shot object recognition.

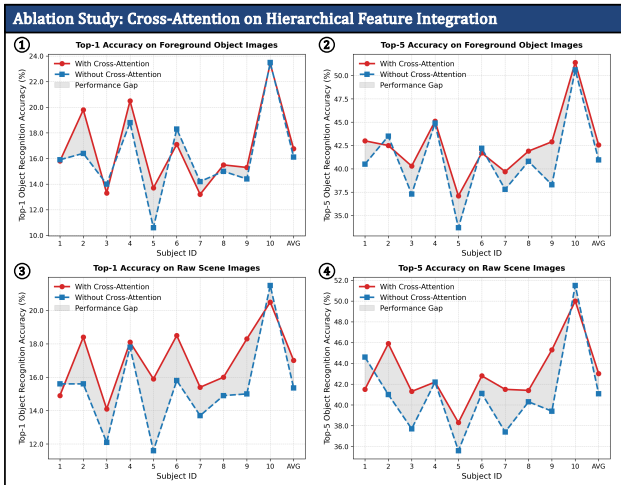


Figure 4: **Impact of cross-attention integration.** Subfigures 1&2 show Top-1/5 accuracy of object embedding (F_f) with/without attention, and subfigures 3&4 show the same metrics for context embedding (F_r).

rations that utilized only one type of embedding at a time: F_b (contour-level), F_f (object-level), and F_r (scene-level). In the subject-dependent setting, F_b achieved 14.2% Top-1 and 41.8% Top-5 accuracy. In contrast, F_f and F_r both improved performance to approximately 22% Top-1 accuracy. These results suggest that while each representation captures distinct neural elements, none is sufficient alone to support optimal decoding performance. Notably, F_f and F_r embeddings, which encode mid-level and high-level visual semantics, outperformed F_b , highlighting the greater salience of semantic and contextual elements in EEG brain decoding.

Ablation on Cross Attention. We further examined the role of cross-attention mechanism in integrating multi-level EEG features across the visual hierarchy. Ablating the cross-attention led to noticeable performance degradation. For instance, in the subject-dependent setting, the Top-1 and Top-5 accuracies dropped from 34.1% and 71.3% to 32.4% and 66.8%, respectively, when cross-attention was removed. In the subject-independent setting, similar trends were observed, with the full ViEEG outperforming the variant without cross-attention by notable margins. These findings underscore the importance of cross-attention for aligning and integrating hierarchical EEG embeddings, thereby enhancing overall model robustness and generalization across sub-

jects. The performance gain is particularly evident in the integration of F_f and F_r , as visualized in Figure 4, where the majority of subjects demonstrate that adding cross-attention for hierarchical visual information integration effectively improves EEG decoding of the integrated features.

4.5 Representational Analysis

Representational Similarity Matrices. To assess the representational consistency of ViEEG, we visualize the representational similarity matrices (RSMs) as heatmaps using Subject 8 from the THINGS-EEG dataset. RSMs reflect pairwise similarities among neural embeddings across visual categories, providing insights into how well each model captures the intrinsic EEG structure. For comparison, RSMs from NICE and ATM are also shown in Figure 6, with additional subjects in supplementary Appendix.

All three models exhibit block-diagonal patterns when test samples are ordered by category, indicating basic class-level separation. However, ViEEG shows noticeably sharper diagonals within each block, reflecting stronger intra-class consistency and more accurate instance-level alignment. For example, in the “Food” category, ViEEG maintains focused diagonal peaks, whereas NICE and ATM produce more diffuse patterns. This suggests ViEEG achieves finer discrimination within categories. In less structured or ambiguous classes such as “Tool,” “Sports,” and “Other,” all models show reduced separability, though ViEEG retains relatively clearer patterns. Overall, ViEEG better preserves both category structure and exemplar specificity, which is crucial for downstream EEG retrieval and classification tasks.

Zero-shot Image Retrieval. We further evaluate ViEEG’s decoding ability through zero-shot image retrieval using different visual embeddings: binary object mask (BOM), foreground object (FO), raw scene (RS), and their concatenation (Triple). As shown in Figure 5, each embedding performs differently based on the visual characteristics of the object. For instance, BOM performs best on simple silhouettes like basketballs, while FO excels for complex scenes like aircraft carriers where background blending challenges other embeddings. Notably, the triple fusion consistently achieves the highest accuracy, leveraging complementary information from all views. This fusion mitigates the weaknesses of individual embeddings and enhances retrieval robustness. Additional examples are provided in supplementary Appendix.

Image Reconstruction. To further assess the visual fidelity of ViEEG’s learned representations, we perform image reconstruction using visual embeddings derived from EEG. As shown in Figure 2, the reconstructed images preserve key semantic information of the original stimuli, including object category, shape, and spatial structure. Notably, ViEEG is capable of reconstructing the foreground object and contour, demonstrating its capacity to capture fine-grained visual features from brain signals. Due to space limitations, more reconstruction examples and implementation details are provided in supplementary Appendix.

5 Conclusion

In this work, we proposed ViEEG, a novel EEG visual decoding framework that emulates the hierarchical structure of human visual perception. By integrating biologically motivated image decomposition with hierarchical EEG encoding and cross-attention fusion, ViEEG captures the progressive flow of visual information from edge detection to semantic and contextual understanding. This design directly addresses the critical issue of hierarchical neural encoded neglect in conventional EEG decoding approaches. Through extensive experiments on the THINGS-EEG and THINGS-MEG datasets, ViEEG significantly outperformed state-of-the-art baselines in both subject-dependent and subject-independent zero-shot recognition. Ablation study further validate the importance of each component. Beyond performance gains, ViEEG offers a cognitively plausible model that strengthens the connection between neuroscience and artificial intelligence. We believe our work advances neuro-inspired learning toward more robust, interpretable, and generalizable BCI systems.

References

- Allen, E. J.; St-Yves, G.; Wu, Y.; Breedlove, J. L.; Prince, J. S.; Dowdle, L. T.; Nau, M.; Caron, B.; Pestilli, F.; Charest, I.; et al. 2022. A massive 7T fMRI dataset to bridge cognitive neuroscience and artificial intelligence. *Nature Neuroscience*, 25(1): 116–126.
- Arcaro, M. J.; and Livingstone, M. S. 2021. On the relationship between maps and domains in inferotemporal cortex. *Nature Reviews Neuroscience*, 22(9): 573–583.
- Bai, Y.; Wang, X.; Cao, Y.-p.; Ge, Y.; Yuan, C.; and Shan, Y. 2023. Dreamdiffusion: Generating high-quality images from brain eeg signals. *arXiv preprint arXiv:2306.16934*.
- Ben-Yishai, R.; Bar-Or, R. L.; and Sompolinsky, H. 1995. Theory of orientation tuning in visual cortex. *Proceedings of the National Academy of Sciences*, 92(9): 3844–3848.
- Bridge, H.; Clare, S.; Jenkinson, M.; Jezzard, P.; Parker, A. J.; and Matthews, P. M. 2005. Independent anatomical and functional measures of the V1/V2 boundary in human visual cortex. *Journal of Vision*, 5(2): 1–1.
- Craik, A.; He, Y.; and Contreras-Vidal, J. L. 2019. Deep learning for electroencephalogram (EEG) classification tasks: a review. *Journal of Neural Engineering*, 16(3): 031001.
- Du, C.; Fu, K.; Li, J.; and He, H. 2023. Decoding visual neural representations by multimodal learning of brain-visual-linguistic features. *IEEE Transactions on Pattern Analysis and Machine Intelligence*, 45(9): 10760–10777.
- Felleman, D. J.; and Van Essen, D. C. 1991. Distributed hierarchical processing in the primate cerebral cortex. *Cerebral Cortex (New York, NY: 1991)*, 1(1): 1–47.
- Fu, H.; Wang, H.; Chin, J. J.; and Shen, Z. 2025. BrainVis: Exploring the bridge between brain and visual signals via image reconstruction. In *ICASSP 2025-2025 IEEE International Conference on Acoustics, Speech and Signal Processing (ICASSP)*, 1–5. IEEE.

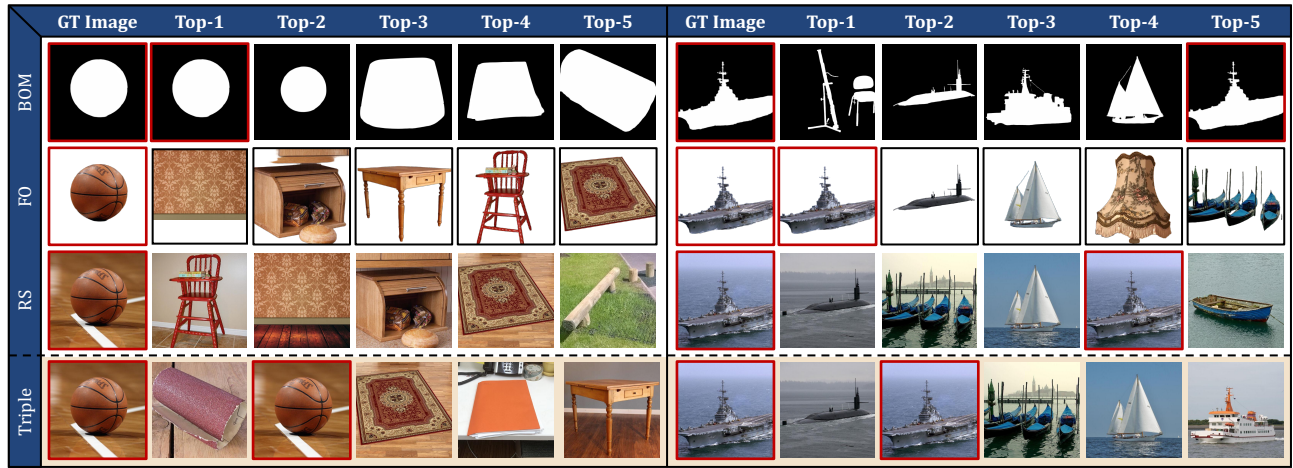


Figure 5: **Zero-shot image retrieval with different embeddings (Subject 8).** Left: basketball example shows BOM excels due to clean contours. Right: aircraft carrier case favors FO due to complex shape and background blending.

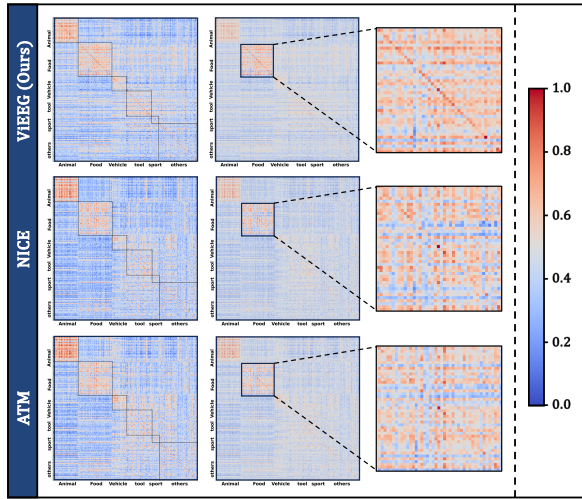


Figure 6: Representational similarity matrices (RSM) across categories (Animal, Food, Vehicle, Tool, Sports, and Others), and zoomed-in view of Food category.

Gifford, A. T.; Dwivedi, K.; Roig, G.; and Cichy, R. M. 2022. A large and rich EEG dataset for modeling human visual object recognition. *NeuroImage*, 264: 119754.

Grill-Spector, K.; and Malach, R. 2004. The human visual cortex. *Annu. Rev. Neurosci.*, 27(1): 649–677.

Hansen, K. A.; Kay, K. N.; and Gallant, J. L. 2007. Topographic organization in and near human visual area V4. *Journal of Neuroscience*, 27(44): 11896–11911.

Hebart, M. N.; Contier, O.; Teichmann, L.; Rockter, A. H.; Zheng, C. Y.; Kidder, A.; Corriveau, A.; Vaziri-Pashkam, M.; and Baker, C. I. 2023. THINGS-data, a multimodal collection of large-scale datasets for investigating object representations in human brain and behavior. *Elife*, 12: e82580.

Hebart, M. N.; Dickter, A. H.; Kidder, A.; Kwok, W. Y.; Corriveau, A.; Van Wicklin, C.; and Baker, C. I. 2019. THINGS:

A database of 1,854 object concepts and more than 26,000 naturalistic object images. *PLOS ONE*, 14(10): 1–24.

Hochreiter, S. 1997. Long Short-term Memory. *Neural Computation MIT-Press*.

Horikawa, T.; and Kamitani, Y. 2017. Generic decoding of seen and imagined objects using hierarchical visual features. *Nature Communications*, 8(1): 15037.

Huo, J.; Wang, Y.; Wang, Y.; Qian, X.; Li, C.; Fu, Y.; and Feng, J. 2024. Neuropictor: Refining fmri-to-image reconstruction via multi-individual pretraining and multi-level modulation. In *European Conference on Computer Vision*, 56–73. Springer.

Lawhern, V. J.; Solon, A. J.; Waytowich, N. R.; Gordon, S. M.; Hung, C. P.; and Lance, B. J. 2018. EEGNet: a compact convolutional neural network for EEG-based brain-computer interfaces. *Journal of Neural Engineering*, 15(5): 056013.

Lee, S.-H.; Lee, M.; and Lee, S.-W. 2020. Neural decoding of imagined speech and visual imagery as intuitive paradigms for BCI communication. *IEEE Transactions on Neural Systems and Rehabilitation Engineering*, 28(12): 2647–2659.

Li, B.; Todo, Y.; and Tang, Z. 2022. Artificial visual system for orientation detection based on Hubel–Wiesel model. *Brain Sciences*, 12(4): 470.

Li, D.; Wei, C.; Li, S.; Zou, J.; Qin, H.; and Liu, Q. 2024. Visual decoding and reconstruction via eeg embeddings with guided diffusion. *The Thirty-eighth Annual Conference on Neural Information Processing Systems*.

Liu, M.; Guan, D.; Zheng, C.; and Zhu, Q. 2025. Multi-Modal Discriminative Network for Emotion Recognition across Individuals. *IEEE Transactions on Cognitive and Developmental Systems*, 1–13.

Liu, X.-H.; Liu, Y.-K.; Wang, Y.; Ren, K.; Shi, H.; Wang, Z.; Li, D.; Lu, B.-L.; and Zheng, W.-L. 2024. EEG2Video: Towards decoding dynamic visual perception from EEG sig-

- nals. *The Annual Conference on Neural Information Processing Systems*, 37: 72245–72273.
- Podell, D.; English, Z.; Lacey, K.; Blattmann, A.; Dockhorn, T.; Müller, J.; Penna, J.; and Rombach, R. 2023. Sdxl: Improving latent diffusion models for high-resolution image synthesis. *arXiv preprint arXiv:2307.01952*.
- Radford, A.; Kim, J. W.; Hallacy, C.; Ramesh, A.; Goh, G.; Agarwal, S.; Sastry, G.; Askell, A.; Mishkin, P.; Clark, J.; et al. 2021. Learning transferable visual models from natural language supervision. In *International Conference on Machine Learning*, 8748–8763. PMLR.
- Rakhimberdina, Z.; Jodelet, Q.; Liu, X.; and Murata, T. 2021. Natural image reconstruction from fmri using deep learning: A survey. *Frontiers in Neuroscience*, 15: 795488.
- Ramesh, A.; Dhariwal, P.; Nichol, A.; Chu, C.; and Chen, M. 2022. Hierarchical text-conditional image generation with clip latents. *arXiv preprint arXiv:2204.06125*, 1(2): 3.
- Riesenhuber, M.; and Poggio, T. 1999. Hierarchical models of object recognition in cortex. *Nature Neuroscience*, 2(11): 1019–1025.
- Schirrmester, R. T.; Springenberg, J. T.; Fiederer, L. D. J.; Glasstetter, M.; Eggensperger, K.; Tangermann, M.; Hutter, F.; Burgard, W.; and Ball, T. 2017. Deep learning with convolutional neural networks for EEG decoding and visualization. *Human Brain Mapping*, 38(11): 5391–5420.
- Scotti, P.; Banerjee, A.; Goode, J.; Shabalin, S.; Nguyen, A.; Dempster, A.; Verlinde, N.; Yundler, E.; Weisberg, D.; Norman, K.; et al. 2023. Reconstructing the mind’s eye: fmri-to-image with contrastive learning and diffusion priors. *Advances in Neural Information Processing Systems*, 36: 24705–24728.
- Shi, N.; Miao, Y.; Huang, C.; Li, X.; Song, Y.; Chen, X.; Wang, Y.; and Gao, X. 2024. Estimating and approaching the maximum information rate of noninvasive visual brain-computer interface. *NeuroImage*, 289: 120548.
- Song, T.; Zheng, W.; Song, P.; and Cui, Z. 2018. EEG emotion recognition using dynamical graph convolutional neural networks. *IEEE Transactions on Affective Computing*, 11(3): 532–541.
- Song, Y.; Liu, B.; Li, X.; Shi, N.; Wang, Y.; and Gao, X. 2024. Decoding Natural Images from EEG for Object Recognition. In *International Conference on Learning Representations*.
- Song, Y.; Zheng, Q.; Liu, B.; and Gao, X. 2022. EEG conformer: Convolutional transformer for EEG decoding and visualization. *IEEE Transactions on Neural Systems and Rehabilitation Engineering*, 31: 710–719.
- Sun, J.; Li, M.; Chen, Z.; Zhang, Y.; Wang, S.; and Moens, M.-F. 2023. Contrast, attend and diffuse to decode high-resolution images from brain activities. *Advances in Neural Information Processing Systems*, 36: 12332–12348.
- Thorpe, S.; Fize, D.; and Marlot, C. 1996. Speed of processing in the human visual system. *Nature*, 381(6582): 520–522.
- Wang, S.; Liu, S.; Tan, Z.; and Wang, X. 2024. Mindbridge: A cross-subject brain decoding framework. In *Proceedings of the IEEE/CVF Conference on Computer Vision and Pattern Recognition*, 11333–11342.
- Wei, Y.; Cao, L.; Li, H.; and Dong, Y. 2024. MB2C: Multi-modal Bidirectional Cycle Consistency for Learning Robust Visual Neural Representations. In *Proceedings of the 32nd ACM International Conference on Multimedia*, 8992–9000.
- Worsley, K. J.; Liao, C. H.; Aston, J.; Petre, V.; Duncan, G.; Morales, F.; and Evans, A. C. 2002. A general statistical analysis for fMRI data. *Neuroimage*, 15(1): 1–15.
- Ye, H.; Zhang, J.; Liu, S.; Han, X.; and Yang, W. 2023. Ip-adapter: Text compatible image prompt adapter for text-to-image diffusion models. *arXiv preprint arXiv:2308.06721*.
- Zafar, R.; Malik, A. S.; Kamel, N.; Dass, S. C.; Abdullah, J. M.; Reza, F.; and Abdul Karim, A. H. 2015. Decoding of visual information from human brain activity: A review of fMRI and EEG studies. *Journal of Integrative Neuroscience*, 14(02): 155–168.
- Zhang, K.; He, L.; Jiang, X.; Lu, W.; Wang, D.; and Gao, X. 2024. CognitionCapturer: Decoding Visual Stimuli From Human EEG Signal With Multimodal Information. *Association for the Advancement of Artificial Intelligence*.
- Zheng, P.; Gao, D.; Fan, D.-P.; Liu, L.; Laaksonen, J.; Ouyang, W.; and Sebe, N. 2024. Bilateral Reference for High-Resolution Dichotomous Image Segmentation. *CAAI Artificial Intelligence Research*, 3: 9150038.
- Zhou, Q.; Du, C.; Wang, S.; and He, H. 2024. CLIP-MUSED: CLIP-Guided Multi-Subject Visual Neural Information Semantic Decoding. *The Annual Conference on Neural Information Processing Systems*.

ViEEG: Hierarchical Visual Neural Representation for EEG Brain Decoding

Supplementary Material: Appendix

6 Details of the Datasets

6.1 THINGS-EEG

We conducted experiments on the large-scale THINGS-EEG dataset (Gifford et al. 2022), designed to support neural decoding of visual object recognition. The dataset contains EEG recordings from ten healthy adult participants (mean age: 28.5 years; 8 female, 2 male), all with normal or corrected-to-normal vision. EEG signals were acquired using a 64-channel (see Figure 7) cap arranged according to the 10–10 international system and sampled at 1000 Hz, with online band-pass filtering between 0.1–100 Hz and referencing to Fz.

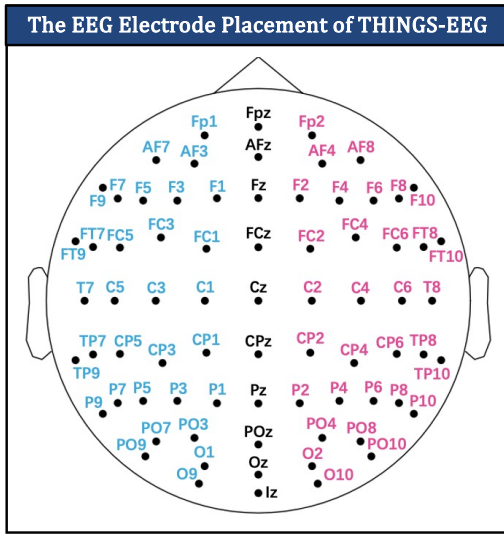


Figure 7: The corresponding EEG electrode placement of THINGS-EEG dataset.

Visual stimuli were selected from the THINGS image database (Hebart et al. 2019), which includes naturalistic object images spanning 1854 distinct concepts grouped into 27 higher-level categories. The THINGS image dataset comprises six major categories, including animals (e.g., cats, dogs), vehicles (e.g., airplanes, ships), food items (e.g., cake, corn), tools (e.g., cameras, phones), sports equipment (e.g., balls, golf clubs), and other miscellaneous categories. For model training and evaluation, these concepts were split into 1654 training and 200 testing categories. Each training concept was associated with ten images, while each test concept had one image. The experiment followed a rapid serial visual presentation (RSVP) paradigm (Thorpe, Fize, and Marlot 1996), where participants viewed 20 images per trial, each presented for 100 ms followed by a 100 ms blank screen (i.e., 200 ms SOA). An orthogonal target detection task was used to maintain attention.

Each participant completed four sessions, resulting in a total of 82,160 trials per subject, including 16,540 training

image trials (each repeated four times) and 200 test images (each repeated 80 times). Trials containing target stimuli were excluded. EEG data were segmented from 200 ms before to 800 ms after stimulus onset, followed by baseline correction and downsampling to 250 Hz. All 64 channels were retained, and signals were averaged across repeated presentations of the same image to enhance signal-to-noise ratio. Following prior work (Song et al. 2024), multivariate noise normalization was applied to the training set. Input images were resized to 224×224 pixels and normalized before being fed into the visual encoder.

6.2 THINGS-MEG

We additionally evaluated our model on the THINGS-MEG dataset (Hebart et al. 2023), which provides magnetoencephalography (MEG) recordings from four participants across 12 sessions. Visual stimuli were drawn from the THINGS database (Hebart et al. 2019), encompassing 1854 object concepts and over 26,000 curated naturalistic images. During each session, participants viewed images for 500 ms followed by a blank interval of 1000 ± 200 ms while maintaining central fixation. An orthogonal oddball detection task was employed to ensure sustained attention.

For zero-shot evaluation, 200 object concepts were held out from the training set. The training set consisted of 1854 concepts, each paired with 12 unique images ($1854 \times 12 \times 1$), and the test set included 200 concepts with one image repeated 12 times ($200 \times 1 \times 12$). MEG data were acquired with a 271-channel whole-head system and epoched from 0 to 1000 ms after stimulus onset. Preprocessing involved band-pass filtering in the 0.1–100 Hz range, baseline correction, and downsampling to 200 Hz. To improve signal stability, we averaged repeated responses for each image. Due to the limited number of participants, statistical analysis was not conducted on this dataset, and it serves as a supplementary validation of the EEG-based findings.

7 Comparison Methods

To validate the efficacy of our proposed approach, we compare ViEEG with some classical and recent methods for EEG cognitive decoding and visual decoding. Below, we provide detailed descriptions of the baseline approaches:

- **BraVL [IEEE TPAMI’2023] (Du et al. 2023):** BraVL employs multimodal learning to jointly model brain, visual, and linguistic features, maximizing intra- and inter-modality mutual information to improve consistency and data efficiency.
- **LSTM (Hochreiter 1997):** Long Short-Term Memory networks are leveraged to capture long-term temporal dependencies in sequential EEG data.
- **ConvNet (Schirrmeyer et al. 2017):** A convolutional neural network designed for end-to-end EEG decoding, focusing on extracting spatial and spectral features directly from raw EEG signals.

Method	Subject 1		Subject 2		Subject 3		Subject 4		Ave	
	top-1	top-5	top-1	top-5	top-1	top-5	top-1	top-5	top-1	top-5
Subject dependent - train and test on one subject										
Conformer (Song et al. 2022)	9.1	27.1	20.8	47.4	15.2	40.7	9.8	27.9	13.7	35.8
DGCNN (Song et al. 2018)	6.7	22.0	14.1	36.2	11.9	35.8	7.7	22.8	10.1	29.2
EEGNet (Lawhern et al. 2018)	9.8	29.2	17.9	48.9	14.8	41.3	9.1	28.7	12.9	37.0
Mb2C (Wei et al. 2024)	9.3	33.6	20.6	49.2	18.2	44.3	10.2	33.6	14.6	39.9
NICE (Song et al. 2024)	11.5	35.6	25.7	54.4	21.0	47.8	11.2	35.2	17.4	43.3
ATM (Li et al. 2024)	8.0	29.3	30.2	61.5	20.3	50.5	11.8	33.3	17.6	43.7
ViEEG	16.6	50.3	37.4	79.1	30.6	73.9	17.2	49.5	25.5	63.2

Table 4: Overall Top-1/5 accuracy (%) on THINGS-MEG for 200-way zero-shot recognition.

- **Conformer [IEEE TNSRE’2022] (Song et al. 2022):** This architecture combines convolutional neural networks with Transformer modules to extract both local and global dependencies in sequential EEG data.
- **DGCNN [IEEE TAFFC’2018] (Song et al. 2018):** The Dynamical Graph CNN employs a learnable adjacency matrix along with Chebyshev filters to capture dynamic relationships for EEG emotion classification.
- **EEGNet (Lawhern et al. 2018):** A lightweight convolutional network that efficiently extracts temporal and spatial features from EEG signals, optimized for BCI applications.
- **MB2C [ACM MM’2024] (Wei et al. 2024):** The Multi-modal Bidirectional Cycle Consistency framework utilizes dual-GAN architectures to generate and reconcile modality-specific features, effectively bridging the modality gap in zero-shot tasks, EEG classification, and image reconstruction.
- **NICE [ICLR’2024] (Song et al. 2024):** A self-supervised framework that learns image representations from EEG by incorporating attention modules to capture spatial correlations within brain activity.
- **ATM [NeurIPS’2024] (Li et al. 2024):** The Adaptive Thinking Mapper projects neural signals into a shared subspace with CLIP embeddings via a two-stage EEG-to-image generation strategy, enabling zero-shot visual decoding and reconstruction.
- **CognitionCapturer (CogCap) [AAAI’2025] (Zhang et al. 2024):** This unified framework enhances EEG signal representations by leveraging multimodal data and modality-specific expert encoders. It employs a diffusion prior to map EEG embeddings to the CLIP space, achieving high-fidelity reconstruction of visual stimuli without requiring fine-tuning.

These methods represent a diverse set of strategies for EEG decoding and visual reconstruction, against which ViEEG is rigorously benchmarked.

8 Experiment in THINGS-MEG Dataset

Due to the limited number of subjects in the THINGS-MEG dataset, we conducted subject-dependent experiments, training and testing separately on each subject. Table 4 reports the 200-way zero-shot recognition results. As shown in Table 4, ViEEG also achieves superior performance on

the THINGS-MEG dataset, outperforming all baselines in both top-1 and top-5 accuracy across subjects. These results demonstrate that our neuroscience-inspired framework is not only effective for EEG-based decoding, but also generalizes well to other neural signals such as MEG, further highlighting the robustness and cross-modality potential of our proposed ViEEG.

9 Whole Results of Ablation Study and Parameter Analysis

Due to space limitations, only partial information is presented in the main text. The complete results of the ablation experiments on Hierarchical Embedding and cross-attention are provided here. Figure 5 shows the object recognition accuracy of Hierarchical Embedding in the full ViEEG, while Figure 6 presents the object recognition accuracy of Hierarchical Embedding in ViEEG without cross-attention.

9.1 Ablation on Hierarchical Embedding

The results presented in Table 5 showcase the performance of different hierarchical EEG feature combinations on object recognition. These results were obtained from ViEEG with the full cross-attention mechanism.

We investigated the impact of three distinct visual embeddings: F_b (contour-based), F_f (foreground-object-focused), and F_r (contextual). Each of these embeddings contributes valuable information, but their individual contributions are limited when used in isolation.

F_b -Only (contour-based embedding) showed moderate performance, with Top-1 accuracy ranging from 14.2% to 17.6% in the subject-dependent setting and 5.9% to 10.2% in the subject-independent setting. The contour-based features alone provide basic structure but lack the granularity needed for high accuracy.

F_f -Only (object-focused embedding) consistently outperformed F_b -Only, with Top-1 accuracy ranging from 22.2% to 38.7% in the subject-dependent setting and 15.8% to 23.4% in the subject-independent setting. The object-focused embedding captures detailed object features, enhancing the model’s ability to distinguish between classes, particularly in controlled settings.

F_r -Only (contextual embedding) also improved performance over F_b -Only, with Top-1 accuracy ranging from 22.1% to 40.6% in the subject-dependent setting and 14.9%

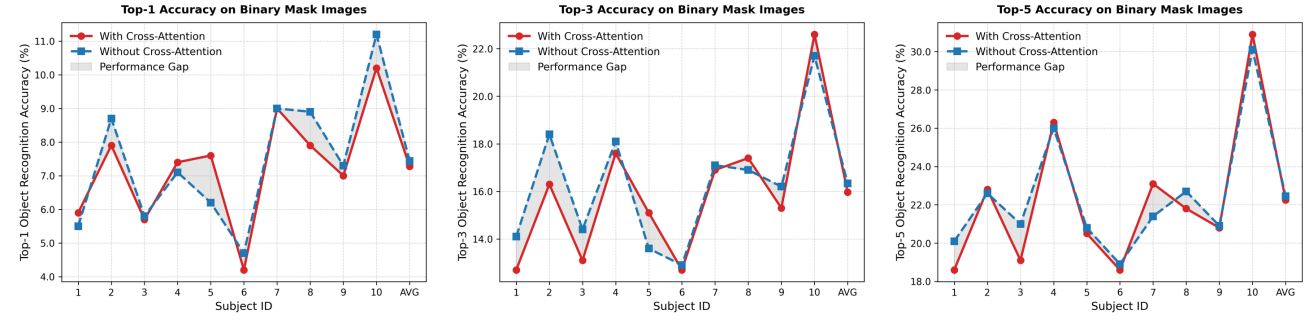
Subject-Dependent Setting													Subject-Independent Setting												
F_b	F_f	F_r	Sub-1	Sub-2	Sub-3	Sub-4	Sub-5	Sub-6	Sub-7	Sub-8	Sub-9	Sub-10	AVG	Sub-1	Sub-2	Sub-3	Sub-4	Sub-5	Sub-6	Sub-7	Sub-8	Sub-9	Sub-10	AVG	
Top-1 Accuracy																									
✓	✗	✗	14.2	14.0	17.0	20.9	8.6	13.6	14.7	17.6	12.8	14.8	14.8	5.9	7.9	5.7	7.4	7.6	4.2	9.0	7.9	7.0	10.2	7.28	
✗	✓	✗	22.2	24.5	29.9	34.0	19.2	32.5	26.5	38.7	29.3	31.8	28.9	15.8	19.8	13.3	20.5	13.7	17.1	13.2	15.5	15.3	23.4	16.76	
✗	✗	✓	22.1	24.8	31.4	33.1	18.5	29.7	26.8	40.6	27.4	31.8	28.6	14.9	18.4	14.1	18.1	15.9	18.5	15.4	16.0	18.3	20.5	17.01	
✓	✓	✗	31.4	32.8	35.0	46.4	25.6	37.5	33.3	46.8	33.8	40.3	36.3	16.8	20.4	12.8	20.1	16.1	16.4	17.8	17.6	16.9	28.4	18.33	
✓	✗	✓	32.2	30.8	35.6	47.5	24.1	38.1	34.9	45.1	32.0	39.6	36.0	16.5	20.5	13.1	20.6	16.0	18.0	17.6	17.6	19.9	27.5	18.73	
✗	✓	✓	25.1	28.8	33.8	39.6	22.0	34.7	28.4	43.0	31.5	33.9	32.1	18.5	21.8	16.7	22.0	19.3	21.3	16.1	18.7	19.8	27.3	20.15	
✓	✓	✓	34.1	38.4	40.6	50.1	28.9	44.3	38.6	54.0	37.3	42.8	40.9	22.7	24.7	19.0	25.5	19.8	20.7	20.9	20.8	23.8	31.2	22.91	
Top-3 object Recognition Accuracy																									
✓	✗	✗	29.8	30.0	29.8	40.1	20.2	28.6	30.6	35.3	26.7	32.9	30.4	12.7	16.3	13.1	17.6	15.1	12.7	16.9	17.4	15.3	22.6	15.97	
✗	✓	✗	41.2	46.0	51.4	58.3	36.6	53.6	45.4	63.3	50.7	58.1	50.5	31.9	34.1	29.4	35.7	28.6	33.6	29.4	32.2	31.5	43.0	32.94	
✗	✗	✓	40.6	46.2	51.5	56.8	36.6	55.9	48.9	65.1	51.3	55.9	50.9	32.8	34.2	31.1	33.1	29.9	35.7	31.2	32.3	35.8	39.1	33.52	
✓	✓	✗	54.3	53.5	57.6	69.9	45.6	60.8	56.7	69.4	56.7	62.0	58.7	33.2	35.0	30.4	39.4	28.5	32.4	33.3	31.1	32.5	47.6	34.34	
✓	✗	✓	56.2	53.4	57.7	68.8	43.5	60.1	57.9	69.7	55.5	63.4	58.6	34.0	38.9	32.7	39.0	31.5	34.1	33.0	32.4	34.2	45.4	35.52	
✗	✓	✓	46.5	50.4	56.3	61.2	40.9	57.8	52.3	68.7	56.0	61.1	55.1	35.2	38.5	34.5	38.3	34.4	36.4	33.8	36.6	38.1	46.3	37.21	
✓	✓	✓	58.3	58.1	62.6	72.2	52.3	66.8	63.2	74.1	62.0	68.9	63.9	43.1	43.2	36.6	45.4	37.2	37.8	38.8	36.9	41.5	51.0	41.15	
Top-5 object Recognition Accuracy																									
✓	✗	✗	41.8	39.8	39.1	53.2	30.3	40.9	40.7	46.4	37.6	44.0	41.4	18.6	22.8	19.1	26.3	20.5	18.6	23.1	21.8	20.8	30.9	22.25	
✗	✓	✗	52.1	56.1	66.0	67.1	50.0	63.5	58.7	73.9	61.8	68.5	61.8	43.0	42.5	40.3	45.1	37.1	41.7	39.7	41.9	42.9	51.4	42.56	
✗	✗	✓	52.6	58.0	62.7	67.4	49.1	66.2	60.1	74.1	62.5	68.6	62.1	41.5	45.9	41.3	42.2	38.3	42.8	41.5	41.4	45.3	50.0	43.02	
✓	✓	✗	64.5	62.7	69.2	78.8	55.5	73.0	69.3	78.1	66.8	72.5	69.0	43.7	45.6	40.2	47.9	38.8	41.3	43.1	39.3	42.8	56.3	43.90	
✓	✗	✓	66.4	63.2	69.7	78.3	54.8	72.7	69.5	79.0	65.2	72.6	69.1	43.9	46.8	42.8	49.1	41.0	41.9	42.0	39.6	46.6	54.5	44.82	
✗	✓	✓	57.8	62.2	68.3	70.8	52.5	66.9	64.7	77.7	66.9	72.0	66.0	45.1	48.1	46.5	46.7	43.7	45.8	45.0	45.5	49.3	56.7	47.24	
✓	✓	✓	71.3	67.9	74.7	80.8	61.5	76.5	75.2	82.5	74.9	79.8	74.5	53.5	52.5	48.4	54.1	47.3	49.3	49.4	46.8	52.7	60.3	51.43	

Table 5: Object recognition accuracy for different hierarchical representation integration in ViEEG with cross-attention module

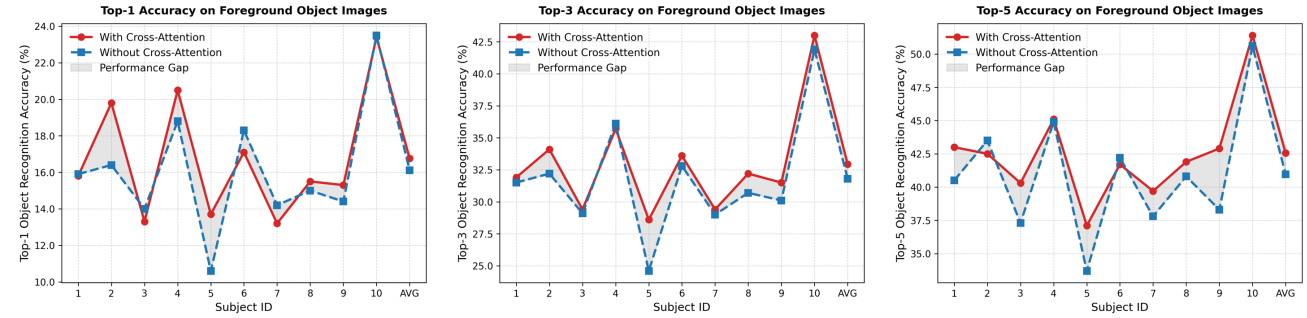
Subject-Dependent Setting													Subject-Independent Setting												
F_b	F_f	F_r	Sub-1	Sub-2	Sub-3	Sub-4	Sub-5	Sub-6	Sub-7	Sub-8	Sub-9	Sub-10	AVG	Sub-1	Sub-2	Sub-3	Sub-4	Sub-5	Sub-6	Sub-7	Sub-8	Sub-9	Sub-10	AVG	
Top-1 Accuracy																									
✓	✗	✗	15.9	14.5	16.0	20.1	9.7	11.3	15.3	17.9	12.0	15.1	14.8	5.5	8.7	5.8	7.1	6.2	4.7	9.0	8.9	7.3	11.2	7.44	
✗	✓	✗	21.4	22.8	28.6	34.6	19.4	26.0	26.8	38.6	21.8	30.8	27.1	15.9	16.4	14.0	18.8	10.6	18.3	14.2	15.0	14.4	23.5	16.11	
✗	✗	✓	21.6	23.2	27.8	33.4	18.9	28.1	25.8	35.6	23.4	32.8	27.1	15.6	15.6	12.1	17.8	11.6	15.8	13.7	14.9	15.0	21.5	15.36	
✓	✓	✗	30.5	30.0	32.9	42.4	24.1	33.7	33.8	46.3	31.6	36.9	34.2	17.9	18.5	12.9	22.7	13.3	17.8	16.5	18.0	17.8	26.7	18.21	
✓	✗	✓	30.0	31.9	32.5	44.2	24.5	34.4	35.4	43.3	31.2	38.1	34.6	17.0	19.6	11.9	19.6	14.4	16.2	15.9	18.0	18.4	26.5	17.75	
✗	✓	✓	24.0	26.2	31.6	38.9	21.9	31.4	27.8	42.7	26.8	35.6	30.7	17.9	18.7	14.8	20.4	13.4	20.3	14.2	17.4	18.1	24.6	17.98	
✓	✓	✓	31.6	33.8	38.3	45.7	26.4	39.7	34.5	51.4	33.8	43.1	37.8	19.1	22.0	15.1	24.2	16.7	21.0	17.2	19.5	20.9	31.1	20.68	
Top-3 object Recognition Accuracy																									
✓	✗	✗	30.6	29.8	28.6	37.9	23.1	26.6	31.3	34.9	29.8	33.8	30.6	13.6	17.9	13.9	17.6	13.1	12.4	16.6	16.4	15.7	21.2	15.84	
✗	✓	✗	38.8	40.1	48.7	55.3	35.7	49.5	46.5	62.6	41.9	55.5	47.5	31.5	32.2	29.1	36.1	24.6	32.8	29.0	30.7	30.1	41.9	31.80	
✗	✗	✓	40.0	44.2	48.3	55.4	36.6	50.7	48.7	60.5	46.5	55.4	48.6	32.3	31.2	28.8	33.9	26.8	31.7	28.3	30.4	29.8	40.5	31.37	
✓	✓	✗	53.4	51.7	56.1	66.8	43.7	56.5	55.1	66.7	53.9	62.0	56.6	34.5	34.3	29.7	38.6	28.1	34.1	30.3	31.9	33.4	45.5	34.04	
✓	✗	✓	54.8	51.8	54.9	67.5	43.0	58.5	57.4	67.8	53.9	61.6	57.1	34.4	32.6	28.8	37.8	27.6	34.7	28.9	31.4	34.2	44.8	33.52	
✗	✓	✓	43.4	47.7	52.4	61.2	40.3	55.5	52.2	67.0	51.2	60.8	53.2	35.8	35.8	31.2	37.8	29.1	36.5	29.9	35.0	34.3	45.9	35.13	
✓	✓	✓	54.3	56.1	60.7	71.4	48.6	62.2	57.6	72.4	59.9	65.1	60.8	39.7	38.5	32.9	43.2	31.4	39.9	33.3	38.0	38.2	49.8	38.49	
Top-5 object Recognition Accuracy																									
✓	✗	✗	41.6	39.8	37.2	51.1	31.6	37.9	42.4	46.1	40.7	46.3	41.5	20.1	22.6	21.0	26.0	20.8	18.9	21.4	22.7	20.9	30.1	22.45	
✗	✓	✗	47.6	52.9	60.7	66.4	47.3	60.0	59.1	71.4	54.8	66.8	58.7	40.5	43.5	37.3	44.9	33.7	42.2	37.8	40.8	38.3	50.6	40.96	
✗	✗	✓	50.4	55.2	59.4	67.4	47.6	61.6	60.4	71.0	60.4	66.0	59.9	44.6	41.0	37.7	42.2	35.6	41.1	37.4	40.3	39.4	51.5	41.08	
✓	✓	✗	65.1	61.9	69.2	78.8	54.6	69.1	66.6	76.3	64.7	72.3	67.9	43.7	43.1	41.9	48.5	36.5	42.6	41.7	40.3	40.8	56.0	43.51	
✓	✗	✓	64.6	59.9	66.4	78.4	55.4	69.5	68.9	75.6	66.5	72.4	67.8	44.7	43.2	39.9	48.6	38.5	43.5	39.1	40.1	43.3	54.5	43.54	
✗	✓	✓	55.9	60.1	64.3	69.4	52.1	65.9	64.6	75.5	63.1	70.2	64.1	47.2	47.8	40.8	47.6	38.5	45.1	41.4	44.4	44.0	53.9	45.07	
✓	✓	✓	66.0	65.1	70.5	79.4	59.0	73.5	70.5	80.0	71.1	74.7	71.0	52.1	48.9	45.1	55.2	41.6	50.4	44.7	45.6	48.8	59.8	49.22	

Table 6: Object recognition accuracy for different hierarchical representation integration in ViEEG without cross-attention module

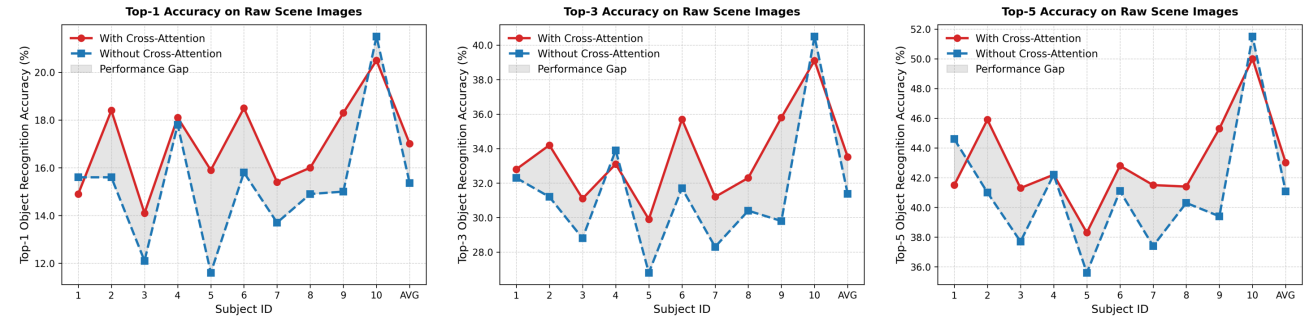
Ablation Study: Binary Mask Visual Embedding F_b (No enhancement via integration)



Ablation Study: Foreground Object Visual Embedding F_f (Enhanced via Contour-to-Object Integration)



Ablation Study: Raw Scene Visual Embedding F_r (Enhanced via Object-to-Context Integration)



Ablation Study: Binary Mask Visual Embedding F_{EEG} (Fusion of F_b , F_f , and F_r)

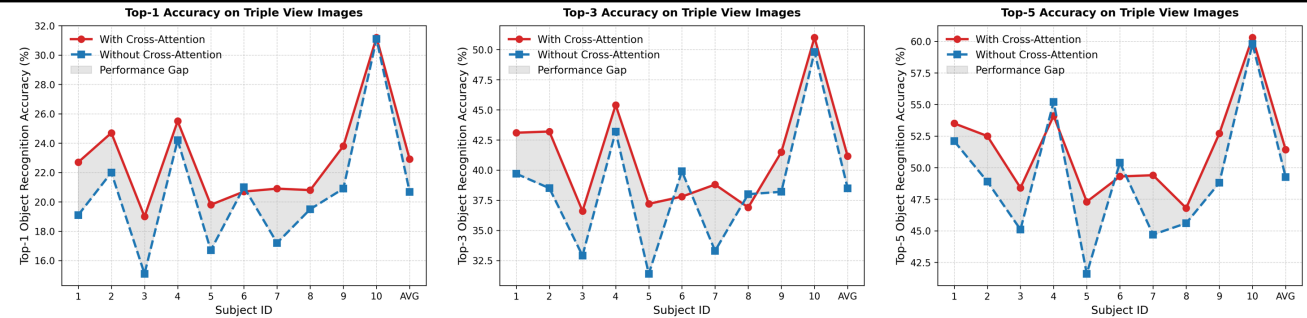


Figure 8: Detailed ablation study of attention on hierarchical visual embeddings in ViEEG.

to 31.8% in the subject-independent setting. Contextual information helps provide broader scene understanding, aiding the model in handling more complex visual stimuli.

When combining all three embeddings (F_b , F_f , and F_r) as F_{EEG} , the model achieved the best results, with Top-1 accuracy reaching 34.1% to 54.0% in the subject-dependent setting and 22.7% to 31.2% in the subject-independent setting. This combination benefits from the strengths of all three feature types, with F_f contributing detailed object-level features, F_r enhancing contextual understanding, and F_b offering contour-based structural information. The complementary nature of these embeddings highlights the importance of integrating multiple types of visual information for effective EEG-based object recognition.

These findings underscore the need for a comprehensive, multi-embedding approach, where each embedding type contributes specific and essential information. Combining these embeddings leads to the most effective hierarchical feature representation, improving both subject-dependent and subject-independent recognition accuracy.

9.2 Ablation on Cross Attention

We further analyzed the effectiveness of the cross-attention module, which is essential for integrating the hierarchical features in ViEEG. Removing the cross-attention component (w/o C-Att) resulted in a noticeable performance drop. In the subject-dependent experiments, the configuration without cross-attention achieved a Top-1 accuracy of 32.4% and Top-5 accuracy of 66.8%, compared to 34.1% and 71.3% for the full ViEEG. In the subject-independent setting, similar trends were observed, with the full model outperforming the variant without cross-attention by significant margins. This highlights the crucial role of cross-attention in aligning and integrating hierarchical EEG embeddings, thereby improving the robustness and generalization of the model across different subjects.

The impact of cross-attention is particularly evident when integrating the different feature embeddings. As illustrated in Figure 4, the addition of cross-attention leads to significant improvements in the EEG decoding of the integrated features, especially for the following:

Binary Mask Visual Embedding F_b : Since this feature was not integrated or enhanced via cross-attention, its performance remains similar to the ablation results. As shown in Table 5, the Top-1 accuracy for F_b -Only is quite low, with values around 14.2% to 17.6% in the subject-dependent setting and 5.9% to 10.2% in the subject-independent setting. This shows that, without cross-attention, the feature alone is insufficient for effective object recognition.

Foreground Object Visual Embedding F_f : This feature benefits from contour-to-object integration, which improves performance but to a smaller extent compared to other more comprehensive features. The Top-1 accuracy for F_f -Only ranged from 22.2% to 38.7% in the subject-dependent setting and 15.8% to 23.4% in the subject-independent setting. Adding cross-attention slightly enhances its performance, demonstrating the importance of cross-attention in boosting object-specific feature extraction.

Raw Scene Visual Embedding F_r : This feature also shows an improvement through object-to-context integration, leading to higher accuracy compared to F_b and F_f . The Top-1 accuracy for F_r -Only ranged from 22.1% to 40.6% in the subject-dependent setting and 14.9% to 31.8% in the subject-independent setting. Cross-attention further improves this performance by aligning the raw scene features with the context, helping the model leverage broader scene information.

Combined Binary Mask Visual Embedding F_{EEG} : The concatenated representation of F_b , F_f , and F_r saw the most significant improvement after adding cross-attention. As seen in the results, this combination achieved a Top-1 accuracy of 34.1% to 54.0% in the subject-dependent setting and 22.7% to 31.2% in the subject-independent setting, which is substantially higher than the individual embeddings. Cross-attention allows for the effective integration of these features, leading to a more comprehensive and robust EEG representation.

In Figure 4, we present line charts that highlight the changes in accuracy before and after the integration of cross-attention for each feature. The four subplots represent the Top-1 and Top-5 accuracy changes for each feature: F_b , F_f , F_r , and F_{EEG} . These subplots illustrate the performance improvements across the subject-dependent and subject-independent settings. The line charts clearly show that, although individual embeddings benefit from cross-attention, the most significant boost is observed when combining all three embeddings. This visualization allows for a clearer comparison of how cross-attention enhances the overall performance of ViEEG across various feature combinations. More detailed results are available in the Appendix for further reference.

9.3 Ablation on EEG Encoder

We conducted a detailed ablation study of EEG Encoder. For ViEEG, the EEG feature encoder plays a crucial role as same as image segmentation, and it is the foundation for further modal alignment. Replacing our EEG encoder modules with other EEG encoders (e.g., ATM (Li et al. 2024) and NICE (Song et al. 2024)) for feature extraction led to an average performance significantly drop, as shown from Table 7 below. Our proposed ViEEG achieves the best performance in every experiment, which demonstrates that the SOTA performance of our method is not only dependent on image segmentation features, but also on the hierarchical EEG Encoder. Moreover, as shown by the “increase” value from tables, our proposed hierarchical visual decoding framework shows a significantly improvement in the accuracy rate of object recognition. Thus, ViEEG’s SOTA performance arises from the synergy between biologically motivated segmentation and hierarchical EEG encoding.

9.4 Ablation on Hierarchical Processing Order

While our framework adopts a bottom-up order (contour \rightarrow object \rightarrow scene) based on visual neuroscience, we also tested other alternative integration orders (e.g., object \rightarrow contour \rightarrow scene, random) in the Table 8. Results show that

Method	Subject 1		Subject 2		Subject 3		Subject 4		Subject 5		Subject 6		Subject 7		Subject 8		Subject 9		Subject 10		Ave	
	top-1	top-5	top-1	top-5	top-1	top-5	top-1	top-5	top-1	top-5	top-1	top-5	top-1	top-5	top-1	top-5	top-1	top-5	top-1	top-5	top-1	top-5
Subject dependent - train and test on one subject																						
LSTM (Hochreiter 1997)	25.8	60.5	23.1	49.3	30.5	60.8	29.6	60.1	20.3	41.2	25.4	51.7	28.5	59.0	30.6	62.0	27.0	53.1	34.8	67.7	27.6	56.5
DGCNN (Song et al. 2018)	18.2	49.1	14.8	43.2	20.5	52.4	29.0	63.2	12.8	38.8	17.8	53.9	20.6	55.4	29.6	65.4	21.7	52.2	26.1	62.4	21.1	53.6
EEGNet (Lawhern et al. 2018)	21.6	55.4	25.3	59.2	25.3	61.2	30.5	67.1	16.4	46.5	26.7	61.3	25.2	58.6	37.1	71.1	26.0	61.2	32.8	67.6	26.7	60.9
NICE (Song et al. 2024)	31.1	66.7	34.2	65.8	38.9	71.2	45.8	79.5	26.7	69.1	40.6	74.3	35.4	70.6	50.2	80.5	35.1	72.3	40.0	75.7	37.8	72.6
ATM (Li et al. 2024)	30.8	67.3	34.8	65.6	36.6	72.3	44.9	80.6	28.2	60.9	37.5	72.2	39.1	74.6	49.3	80.9	34.2	71.6	40.7	77.8	37.6	72.4
CogCap (Zhang et al. 2024)	30.2	65.6	33.1	64.1	37.4	70.8	43.8	78.9	25.7	57.4	34.6	63.5	35.9	71.1	48.7	78.8	35.6	70.3	38.2	76.5	36.3	69.7
ViEEG	34.1	71.3	38.4	67.9	40.6	74.7	50.1	80.8	28.9	61.5	44.3	76.5	38.6	75.2	54.0	82.5	37.3	74.9	42.8	79.8	40.9	74.5
Subject independent - leave one subject out for test																						
LSTM (Hochreiter 1997)	14.8	38.1	13.8	32.5	8.0	24.6	13.0	35.8	10.2	27.6	12.2	32.6	8.5	26.5	14.3	38.8	6.5	28.2	14.1	37.4	11.5	32.2
DGCNN (Song et al. 2018)	12.9	36.5	17.5	39.3	6.3	25.5	12.8	31.0	9.2	32.0	13.7	36.9	7.3	28.8	14.3	32.8	14.2	36.4	15.6	41.3	12.4	34.1
EEGNet (Lawhern et al. 2018)	13.5	36.2	15.9	40.7	7.6	27.8	16.0	37.4	10.3	30.0	12.2	38.2	8.9	29.5	16.8	39.5	10.5	30.6	21.2	51.0	13.3	36.1
NICE (Song et al. 2024)	18.4	50.3	21.9	47.3	14.5	44.6	22.1	53.9	15.0	39.8	20.2	48.4	16.3	43.1	18.4	44.6	19.7	45.2	27.8	45.5	19.4	46.3
ATM (Li et al. 2024)	20.7	48.0	22.2	49.6	14.3	39.6	20.5	48.2	18.2	43.0	18.0	44.1	20.5	42.3	21.6	46.3	19.1	41.6	27.2	55.7	19.8	45.8
CogCap (Zhang et al. 2024)	19.1	47.4	17.1	44.5	10.2	29.0	20.3	44.2	11.2	32.9	17.3	38.6	15.3	35.5	17.4	39.7	13.8	38.8	22.5	50.6	16.4	40.1
ViEEG	22.7	53.5	24.7	52.5	19.0	48.4	25.5	54.1	19.8	47.3	20.7	49.3	20.9	49.4	20.8	46.8	23.8	52.7	31.2	60.3	22.9	51.4

Table 7: Ablation study of EEG encoder: Top-1/Top-5 object recognition accuracy(%).

Method	Subject 1		Subject 2		Subject 3		Subject 4		Subject 5		Subject 6		Subject 7		Subject 8		Subject 9		Subject 10		Ave	
	top-1	top-5	top-1	top-5	top-1	top-5	top-1	top-5	top-1	top-5	top-1	top-5	top-1	top-5	top-1	top-5	top-1	top-5	top-1	top-5	top-1	top-5
Subject dependent - train and test on one subject																						
contour→context→object	34.2	70.6	37	68.2	36.8	73.3	47.6	81.8	28.6	61.0	41.8	75.4	39.7	73.8	53.2	81.3	36.3	73.1	42.7	77.9	39.7	73.6
object→contour→context	34.9	68.0	34.5	67.6	39.3	74.2	47.3	79.1	27.7	60.9	42.6	75.1	39.6	75.7	52.5	81.5	37.2	63.1	42.7	77.0	39.8	72.2
object→context→contour	34.4	69.4	35.8	67.8	40.2	74.1	46.9	79.0	28.3	62.7	40.2	72.6	40.2	75.3	54	80.5	37.5	76.1	43.6	77.8	40.1	73.5
context→contour→object	35.2	69.5	36.5	67.0	40.6	76.2	47.4	78.3	28.5	60.9	42.6	74.4	39.9	74.5	52.4	81.2	35.6	74.8	44.7	78.2	40.3	73.5
context→object→contour	33.8	67.7	37.2	66.9	38.4	74.0	45.5	79.0	31.1	61.7	40.9	74.9	38.3	74.9	53.8	81.0	36.2	73.5	45.2	80.1	40.0	73.3
contour→object→context (ViEEG)	34.1	71.3	38.4	67.9	40.6	74.7	50.1	80.8	28.9	61.5	44.3	76.5	38.6	75.2	54.0	82.5	37.3	74.9	42.8	79.8	40.9	74.5
Subject independent - leave one subject out for test																						
contour→context→object	19.5	50.2	24.9	50.3	15.7	45.6	25.6	52.2	20.9	43.7	19.9	49	17.4	46.5	20.6	46.8	21.6	49.1	29.1	64.8	21.5	49.8
object→contour→context	21.4	53.3	23.7	52.3	18.9	49.6	25.6	54.2	16.4	45.6	20.5	47.7	19.5	47.8	21.5	43.6	22.3	54.6	30.1	63.4	21.9	51.2
object→context→contour	19.8	51.3	24.5	52.8	18.5	49.3	26.3	54.7	20.5	45.7	20.7	48.1	18.5	44.9	18.9	44.7	20.1	54.7	30.7	61.2	21.8	50.7
context→contour→object	21.6	51.8	24.6	51.9	17.4	48.0	25.7	55.9	20.0	45.2	21.1	49.6	20.2	47.2	20.6	44.1	22.3	52.7	30.0	59.9	22.3	50.6
context→object→contour	20.8	51.4	25.9	52.0	18.8	49.4	26.2	54.6	19.0	46.1	21.4	48.5	18.7	45.3	20.8	45.0	22.8	51.6	29.7	60.8	22.4	50.4
contour→object→context (ViEEG)	22.7	53.5	24.7	52.5	19.0	48.4	25.5	54.1	19.8	47.3	20.7	49.3	20.9	49.4	20.8	46.8	23.8	52.7	31.2	60.3	22.9	51.4

Table 8: Ablation study of hierarchical processing order: Top-1/Top-5 object recognition accuracy(%).

the biologically inspired order consistently outperforms others, suggesting that respecting the natural visual hierarchy better aligns EEG features with semantic structure.

9.5 Parameter Analysis of Attention Modules

We conducted a detailed parameter analysis on the attention module in ViEEG, focusing on two key parameters: the number of attention layers and the number of attention heads. In our experiments, we recorded Top-1, Top-3, and Top-5 accuracies. For the layer analysis, we experimented with configurations ranging from 0 to 5 layers. In the within-subject object recognition task, a single attention layer yielded the best performance, significantly outperforming the no-attention baseline. Although configurations with 3 or 4 layers occasionally produced slightly higher Top-3 and Top-5 accuracies in the cross-subject task, the performance differences were negligible while incurring a substantial increase in training parameters. Hence, we adopt a single-layer attention architecture for its optimal balance between performance and computational cost.

For the head analysis, we evaluated five settings (1, 2, 3, 4, and 6 heads). While a configuration with 1 head also achieved acceptable performance, using 3 attention heads consistently provided superior results across all metrics. In the cross-subject setting, the influence of head number was less pronounced, suggesting that the head configuration is less critical for subject-independent generalization. Overall,

our findings support the use of a simplified attention module with 1 layer and 3 heads in ViEEG, effectively enhancing feature integration without unnecessary complexity.

10 Representational Analysis

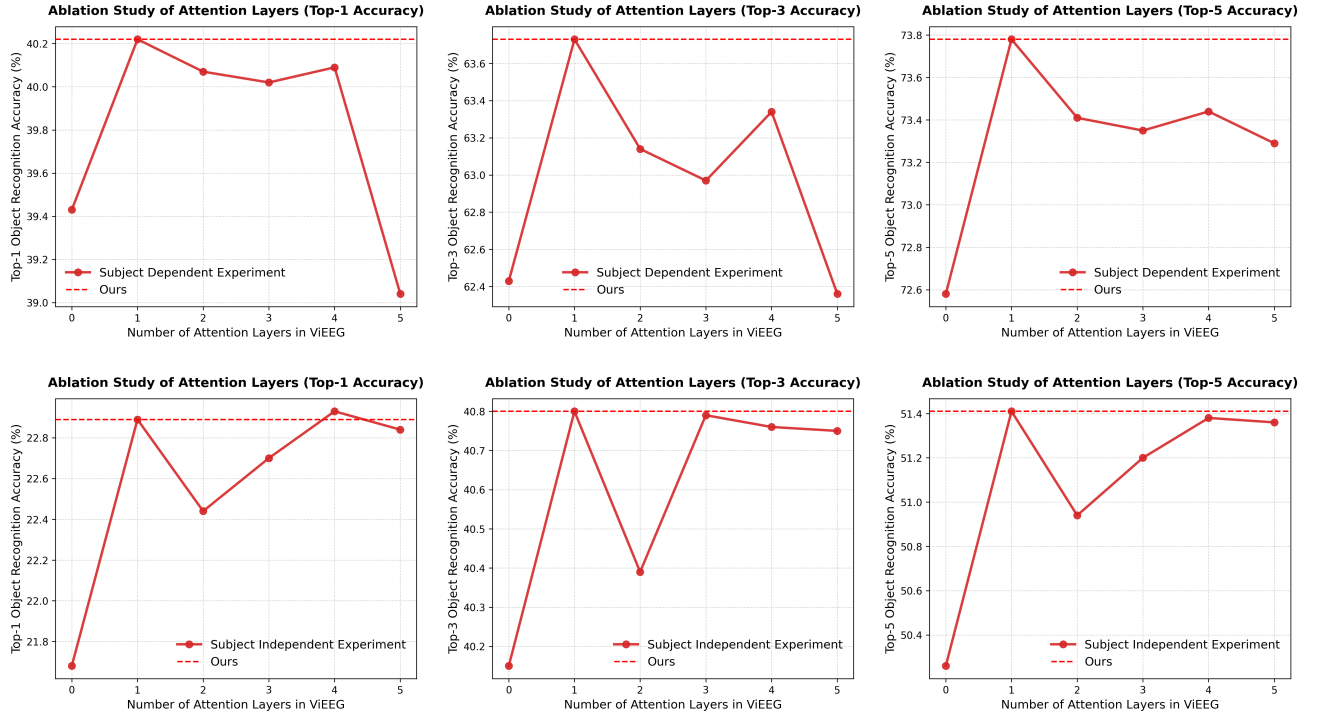
To further support the analysis in the main text, we visualize the representational similarity matrices (RSMs) of ViEEG, NICE (Song et al. 2024), and ATM (Li et al. 2024) across the first six subjects from the THINGS-EEG dataset, as shown in Figure 10. Each matrix reflects how well different EEG conditions are organized in the learned representation space.

Compared to NICE and ATM, ViEEG consistently exhibits sharper diagonal structures across subjects—especially in categories with dense intra-class variation like Food and Animals—indicating better clustering and internal consistency. In contrast, categories such as Tool and Sports appear more scattered in all methods, likely due to inherent category ambiguity. This figure complements our main analysis by highlighting the stability of ViEEG across individuals.

11 Model Computing Resource Comparison

Table 9 presents an integrated analysis of computational requirements and recognition performance. The comparison reveals three key insights through the following aspects:

Parameter Analysis: The Layers Number of Cross-Attention



Parameter Analysis: The Heads Number of Cross-Attention

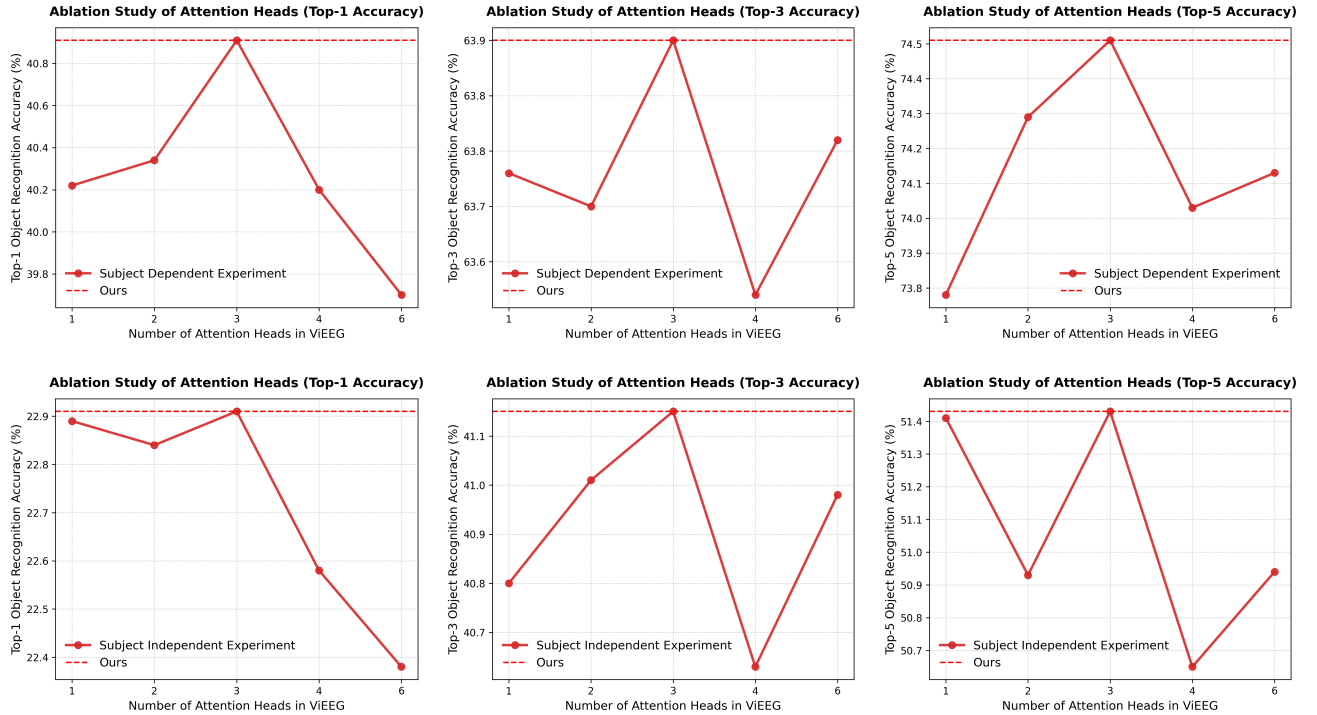


Figure 9: **Parameter analysis of attention modules in ViEEG.** Top row: Performance trends (Top-1, Top-3, Top-5 accuracies) for varying numbers of attention layers under subject-dependent and subject-independent settings. Bottom row: Performance trends for different numbers of attention heads under the same settings.

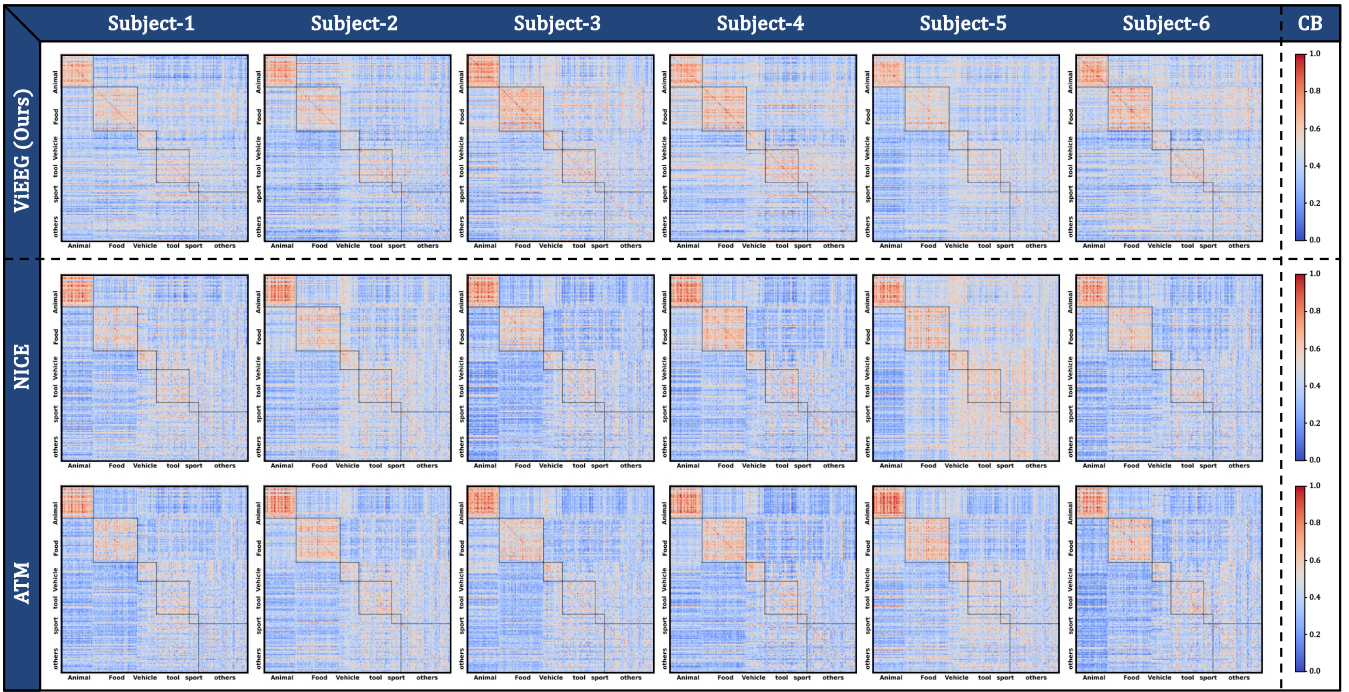


Figure 10: Representational similarity matrices across first six subjects: ViEEG vs. NICE vs. ATM (CB: Color bar).

Methods	FLOPs.	Param.	Train time (s)	Test time (s)
NICE	42.7354 M	2630.940 K	0.0412	0.0058
ATM	98.209 M	3072.662 K	0.0524	0.0088
CopCap	178.973 M	2954.073 K	0.0591	0.0056
ViEEG	127.973 M	7924.488 K	0.0682	0.0062

Table 9: Comprehensive comparison of computational requirements and efficiency.

Computational Efficiency and Accuracy Balance: CopCap achieves the highest baseline accuracy (33.3% Top-1/60.5% Top-5) but requires significantly more computations than other methods, with 179.0M FLOPs – over three times that of NICE (42.7M FLOPs, 27.3% Top-1). Our ViEEG demonstrates a balanced design: while using 28% fewer computations than CopCap (128.0M vs 179.0M FLOPs), it achieves a remarkable 40.9% Top-1 accuracy (7.6% improvement). Notably, ViEEG maintains competitive inference speed (6.2ms), being only marginally slower than CopCap’s 5.6ms despite substantial accuracy gains.

Parameter Utilization Effectiveness: The parameter counts reflect distinct design strategies: NICE (2.63M parameters) prioritizes lightweight design but limits performance (27.3% Top-1). CopCap (2.95M parameters) slightly increases parameters to improve temporal modeling (33.3% Top-1). ViEEG (7.92M parameters) strategically allocates parameters to hierarchical components, enabling multi-scale EEG feature integration. This design yields 74.5% Top-5 accuracy (+14% over CopCap), validating our spatial-frequency interaction mechanism.

Practical Deployment Considerations: ViEEG main-

tains practical efficiency across metrics: Training time per step (68.2ms) shows only moderate increase compared to CopCap (59.1ms). Inference latency (6.2ms) closely matches fastest baselines (NICE:5.8ms, CopCap:5.6ms). Accuracy superiority: Achieves 13.6% Top-1 improvement over NICE with negligible 0.4ms inference delay. The results validate that ViEEG successfully balances model capacity and efficiency through its hierarchical architecture, delivering state-of-the-art performance while maintaining practical deployment feasibility.

The results demonstrate ViEEG’s ability to convert increased parameters into significant accuracy enhancements (40.9% vs 33.3% Top-1) while avoiding excessive computational costs. Compared to CopCap’s 179.0M FLOPs, ViEEG reduces computations by 51.0M FLOPs (equivalent to 28.5% reduction) while improving Top-1 accuracy by 7.6%, showing superior efficiency-accuracy trade-off. The test time comparison further confirms that ViEEG’s accuracy gains (74.5% vs 60.5% Top-5) come without sacrificing real-time processing capability, making it suitable for practical brain signal analysis applications.

12 Image Retrieval Results of ViEEG

To provide further insight into the effectiveness of our multi-embedding retrieval strategy, we visualize the zero-shot image retrieval results from Subject 8 in the THINGS-EEG dataset. For each sample, we present the Top-10 retrieval results using four visual embeddings: binary object mask (BOM), foreground object (FO), raw scene (RS), and their concatenated form (Triple embedding), as shown in Figure 11, Figure 12, Figure 13, and Figure 14, respectively.

The retrieval results reveal that each embedding modality

Method	SSIM \uparrow	Alex(2) \uparrow	Alex(5) \uparrow	Incep \uparrow	CLIP \uparrow	EffNet-B \downarrow	SwAV \downarrow
NICE (Song et al. 2024)	0.353	0.774	0.87	0.736	0.789	0.825	0.588
ATM (Li et al. 2024)	0.351	0.779	0.873	0.745	0.792	0.823	0.591
CogCap (Zhang et al. 2024)	0.346	0.768	0.866	0.737	0.781	0.832	0.595
ViEEG	0.356	0.787	0.881	0.748	0.798	0.811	0.584

Table 10: Quantitative assessments of reconstruction quality.

has its own strengths under different conditions. BOM performs best when the object has simple and distinctive contours (e.g., balls, cones), where boundary information alone is sufficient for recognition. FO excels when object is visually entangled with the background—such as small or embedded items—where isolating the foreground is critical for accurate decoding. RS generally offers robust performance across diverse scenarios, particularly when scene-level semantics are dominant and image embedding is distinctive.

Most notably, the Triple embedding consistently outperforms individual modalities. This is likely due to the complementary nature of the three features—when at least one embedding retrieves a confident match, the corresponding similarity dominates the joint representation, outweighing the weaker or noisy responses from other embeddings. This fusion mechanism effectively boosts retrieval robustness and increases the likelihood of locating the correct object within the Top-5 predictions.

This multi-perspective retrieval approach is also more aligned with the way the human visual system processes complex stimuli: integrating shape, object, and contextual cues for robust perception. Overall, these results reinforce the reliability of ViEEG’s hierarchical decoding framework and highlight the advantages of combining diverse visual representations for EEG-based object recognition.

13 Image Reconstruction Results of ViEEG

13.1 Stable Diffusion XL and IP-Adapter

To enable high-quality image reconstruction from EEG, we leverage Stable Diffusion XL (SDXL) (Podell et al. 2023), a state-of-the-art generative model known for its ability to produce photorealistic and semantically rich images. To bridge the modality gap between neural signals and visual content, we incorporate the IP-Adapter (Ye et al. 2023), which employs dual cross-attention modules to inject conditioning information into the denoising process. Specifically, we use CLIP-ViT-H/14⁷ (Radford et al. 2021) to encode image representations, enabling them to effectively influence the denoising path within the SDXL, thus guiding the model toward more precise and semantically coherent outputs.

For improved inference speed, we utilize SDXL-Turbo⁸, a streamlined version of SDXL optimized for rapid image generation. This variant maintains high visual fidelity while significantly reducing generation latency, making it well-suited for time-sensitive scenarios such as real-time brain signal decoding and neural interface applications.

⁷<https://huggingface.co/laion/CLIP-ViT-H-14-laion2B-s32B-b79K>

⁸<https://huggingface.co/stabilityai/sdxl-turbo>

13.2 Image Reconstruction Results of ViEEG

We present additional image reconstruction results from ViEEG on the THINGS-EEG dataset, as shown in Figure 17, Figure 16, and Figure 15. The figures illustrate the reconstruction results in three semantic categories: vehicles, food, and animals. Overall, ViEEG successfully reconstructs images that maintain semantic consistency with the original stimuli. For example, in Figure 17 (vehicles), reconstructed images effectively capture key structural and shape features of cars, airplanes, and boats. Similarly, Figure 16 (food items) shows that ViEEG can generate food-related textures and shapes, demonstrating its ability to retain category-level information. In Figure 15 (animals), the model reconstructs recognizable features such as fur textures and body structures, reflecting a strong alignment with the original stimuli.

However, certain semantic inconsistencies are observed in some cases. For instance, in Figure 15, when the original image is a cat, some reconstructions depict human faces. This could be due to EEG-induced associative activations, where the subject subconsciously links cats to human interactions. Additionally, errors may arise from attention fluctuations during EEG recording, leading to unintended noise in brain activity. These cases highlight potential challenges in EEG visual decoding, emphasizing the need for further refinement in feature alignment and reconstruction fidelity.

13.3 Quantitative Metrics of Reconstructed Image

We now provide quantitative evaluation of EEG-to-image reconstruction in Table 10, including standard metrics used in prior work (e.g., ATM (Li et al. 2024)). These include:

- **SSIM:** measures low-level structural similarity (e.g., texture, edges);
- **AlexNet (2/5) and Inception:** assess mid/high-level perceptual feature similarity;
- **CLIP:** evaluates alignment in joint vision-language space, relevant for semantic fidelity;
- **EffNet and SwAV:** capture feature compactness and unsupervised visual consistency.

Although the same diffusion model is used, ViEEG achieves consistently better scores due to improved EEG-CLIP alignment. This suggests that our hierarchical EEG encoder contributes to more semantically faithful reconstructions.

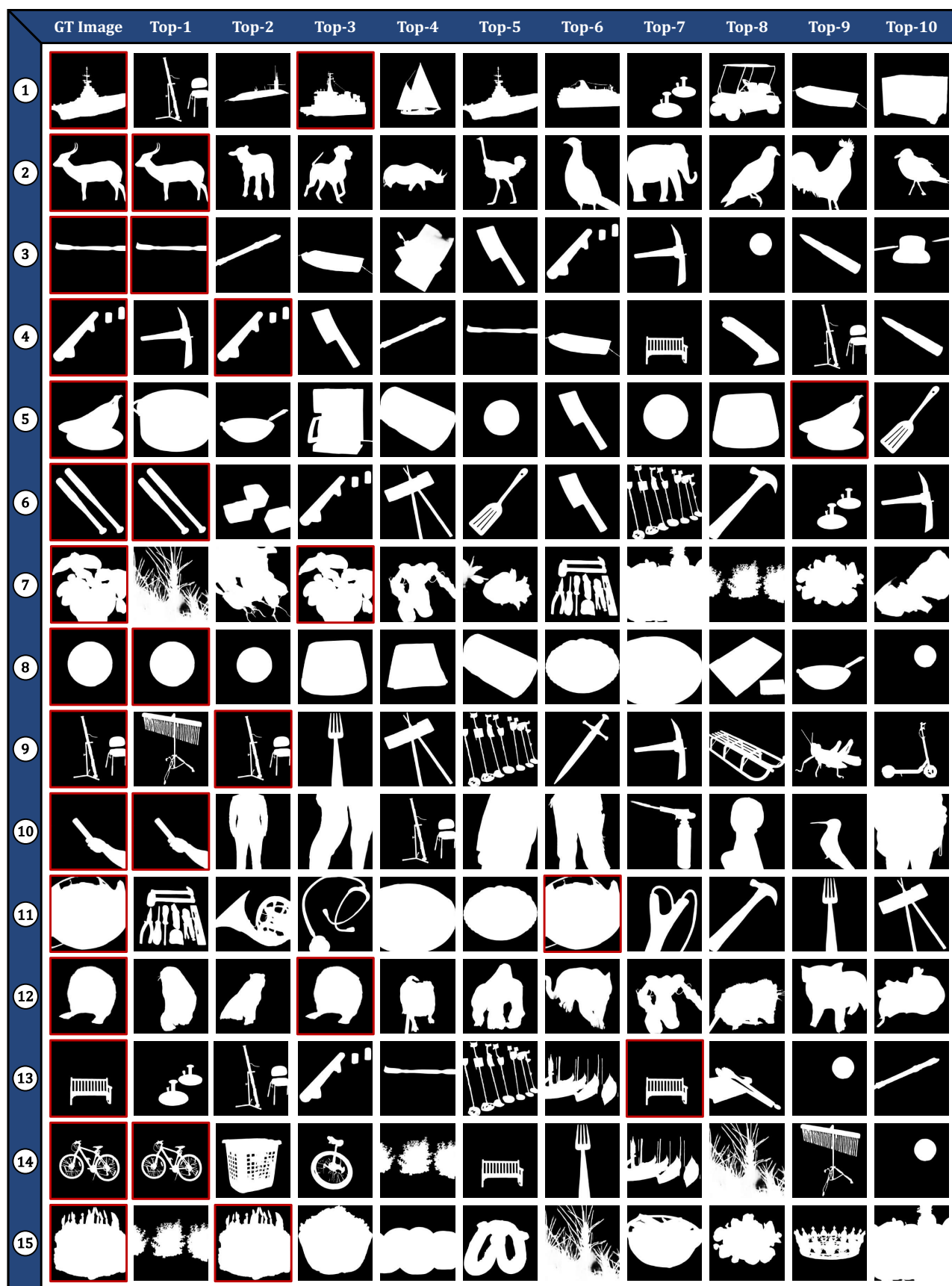


Figure 11: Zero-shot image retrieval results for 15 test samples using binary object mask (BOM) embeddings (Visualizations of the Top-10 retrievals for Subject-8 using binary contour-based EEG-to-image features).

	GT Image	Top-1	Top-2	Top-3	Top-4	Top-5	Top-6	Top-7	Top-8	Top-9	Top-10
1											
2											
3											
4											
5											
6											
7											
8											
9											
10											
11											
12											
13											
14											
15											

Figure 12: Zero-shot image retrieval results for 15 test samples using foreground object (FO) embeddings (Visualizations of the Top-10 retrievals for Subject-8 using EEG features aligned with foreground object representations).

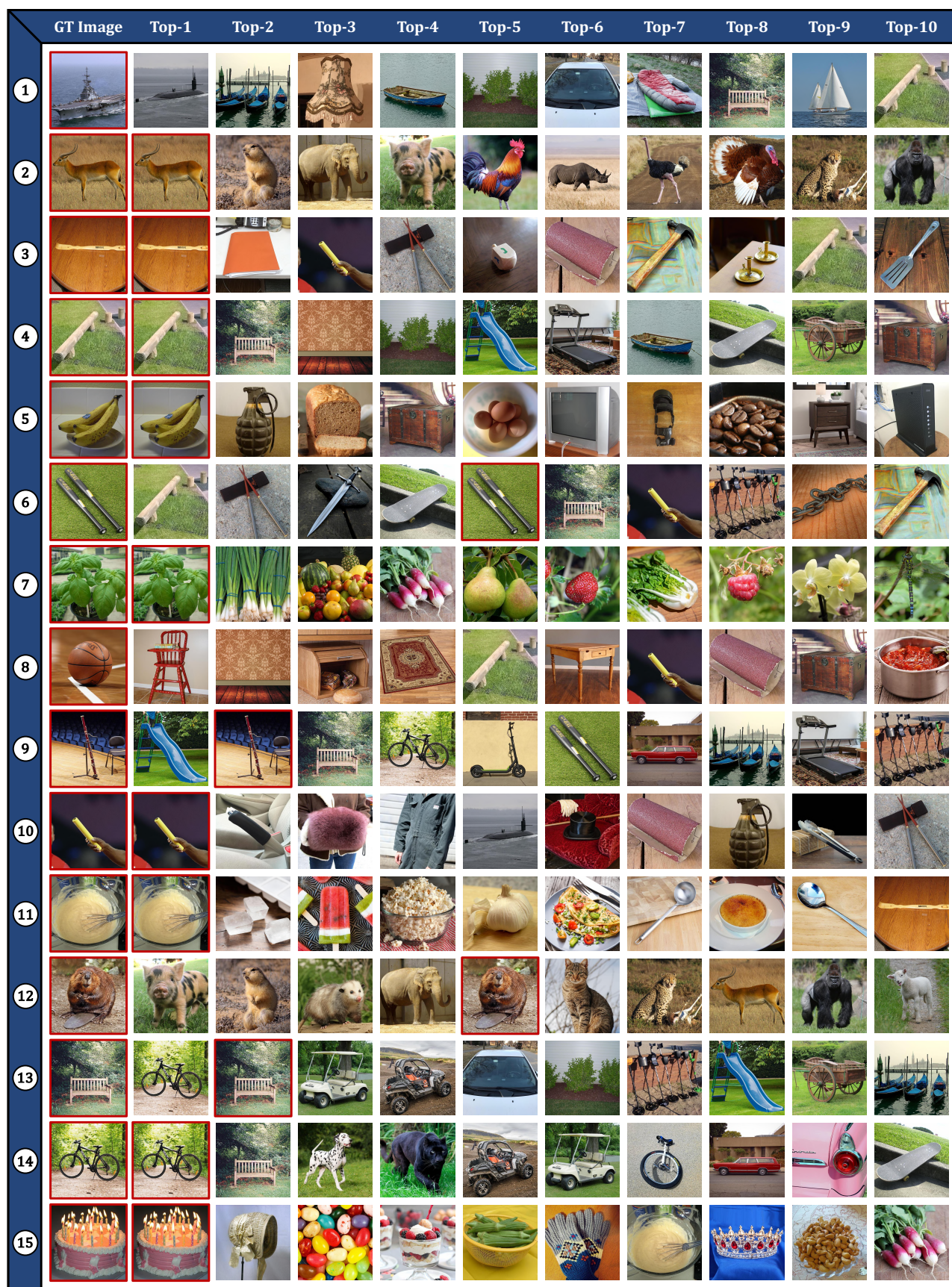


Figure 13: Zero-shot image retrieval results for 15 test samples using raw scene (RS) embeddings (Visualizations of the Top-10 retrievals for Subject-8 based on full-scene EEG-to-image alignment).

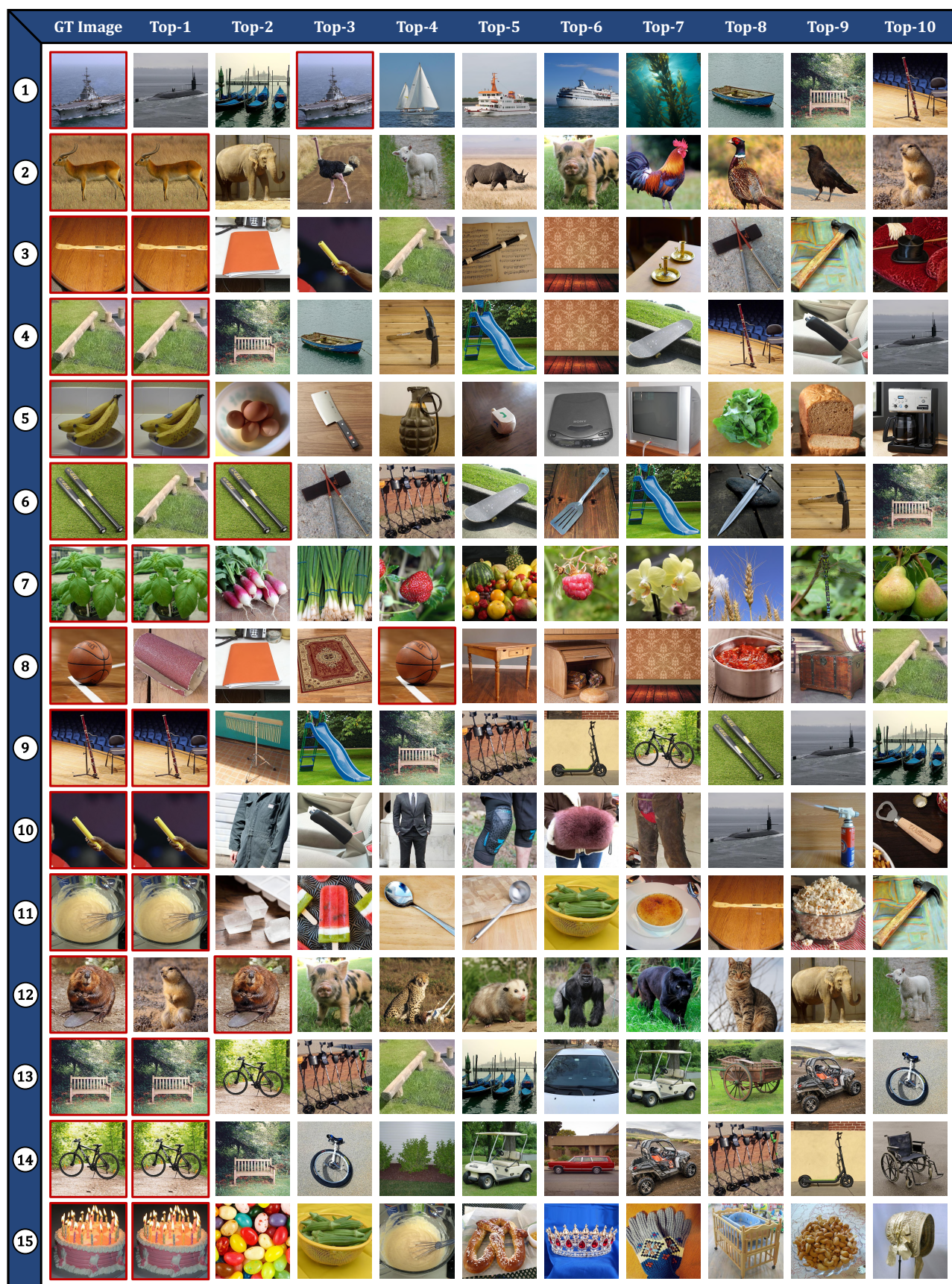


Figure 14: Zero-shot image retrieval results for 15 test samples using triple embedding fusion (BOM + FO + RS) (Visualizations of the Top-10 retrievals for Subject-8 using concatenated multi-scale EEG embeddings).

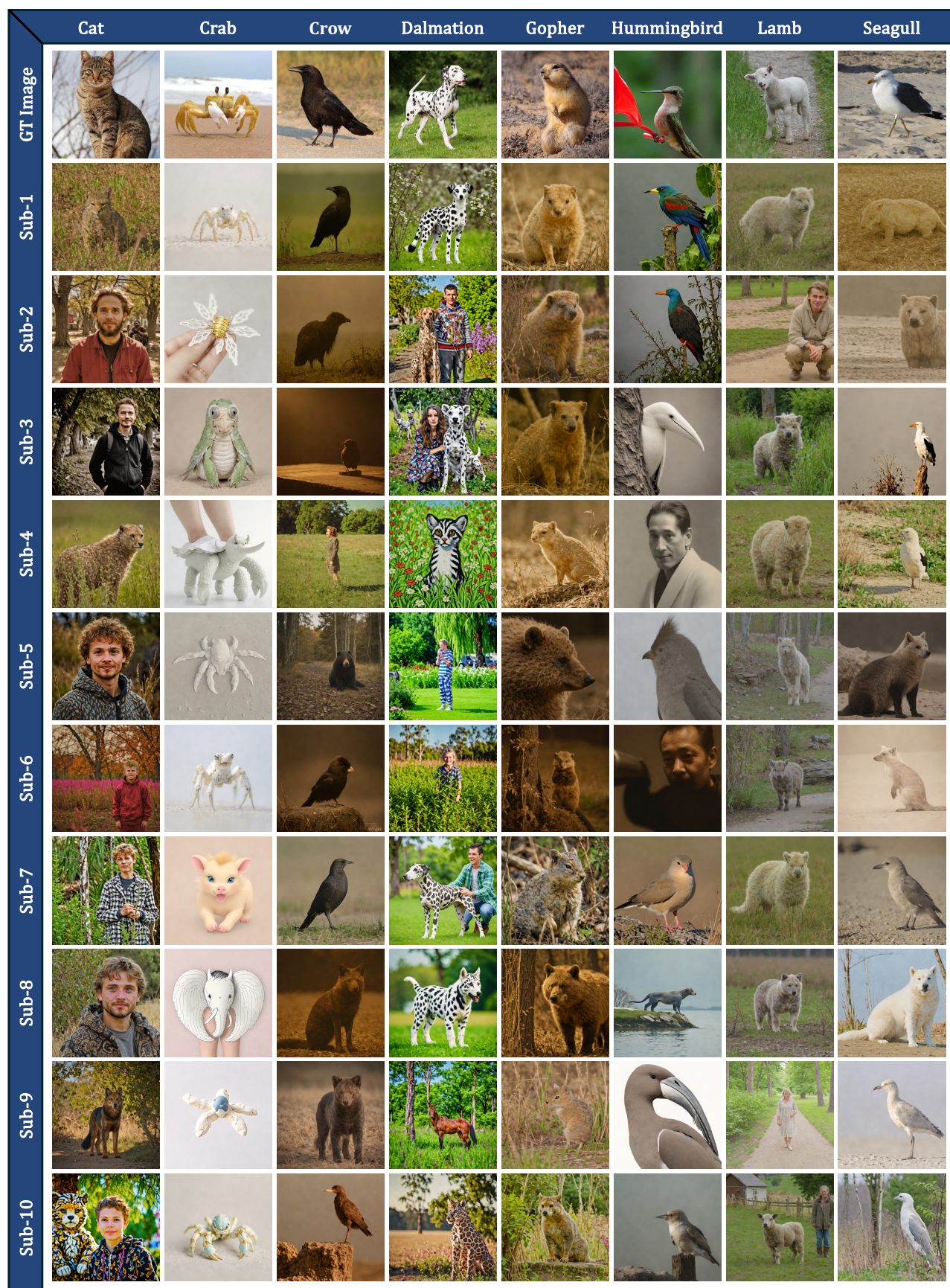


Figure 15: Reconstructed images of animals items using ViEEG.



Figure 16: Reconstructed images of foods items using ViEEG.

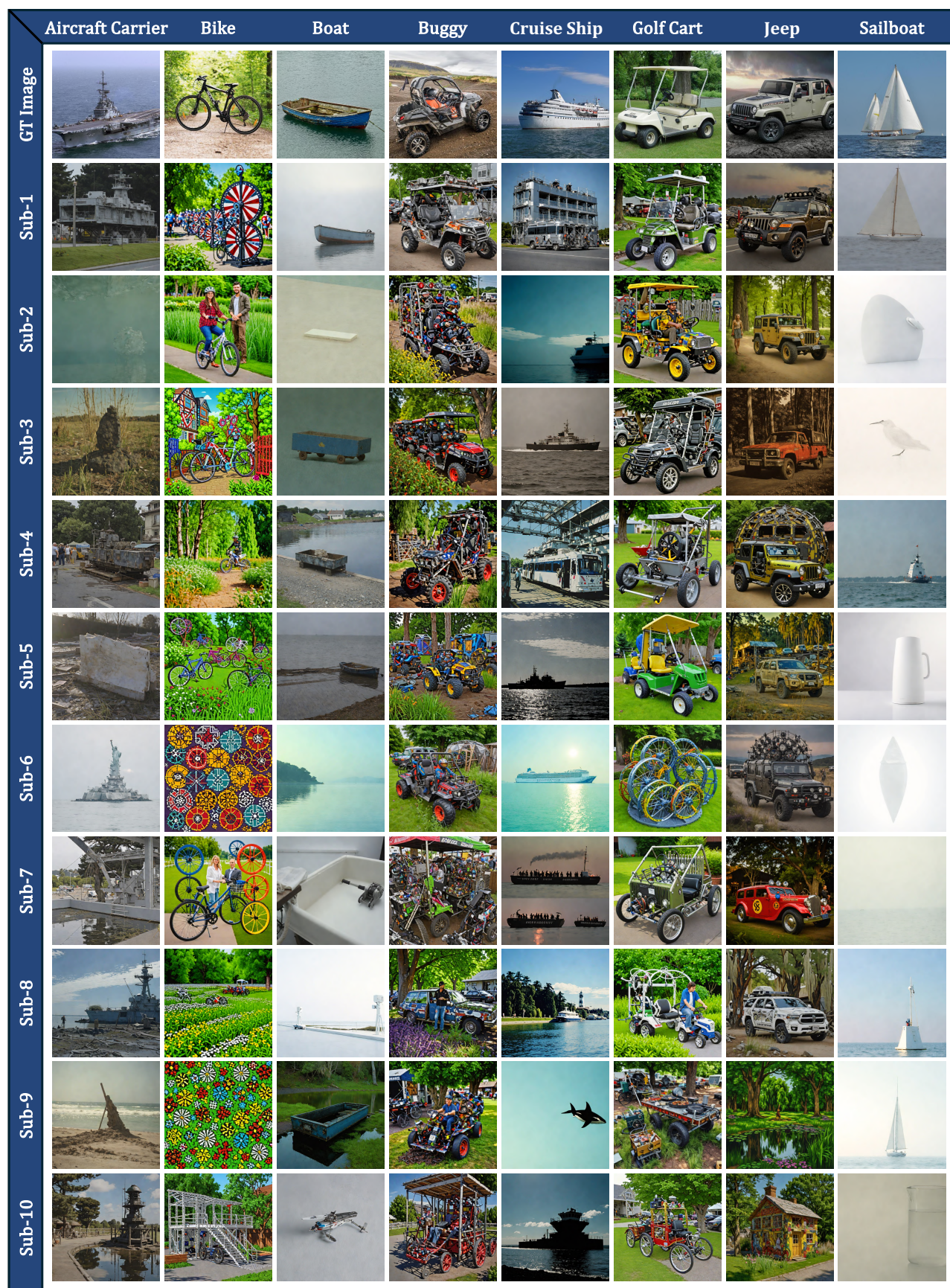


Figure 17: Reconstructed images of vehicles items using ViEEG.